The coexistence of gravity waves from diverse sources during a SOUTHTRAC flight

P. Alexander[1], A. de la Torre[2], P. Llamedo[2], R. Hierro[2], T. Marcos[2], B. Kaifler[3], N. Kaifler[3], M. Geldenhuys[4], A. Giez[5], M. Rapp[3]and J. L. Hormaechea [6]

[1]Instituto de Física de Buenos Aires, CONICET, Ciudad Universitaria Pabellón 1, 1428 Buenos Aires, Argentina
[2]LIDTUA, Facultad de Ingeniería, Universidad Austral and CONICET, 1629 Pilar, Provincia de Buenos Aires, Argentina
[3]Institute of Atmospheric Physics, German Aerospace Center, Oberpfaffenhofen, Germany
[4]Institute of Energy and Climate Research (IEK-7), Forschungszentrum Jülich, Jülich, Germany
[5]Einrichtung Flugexperimente, German Aerospace Center, Oberpfaffenhofen, Germany
[6]Estación Astronómica Río Grande, Facultad de Ciencias Astronómicas y Geofísicas, Universidad Nacional de La Plata and CONICET, Argentina

Key Points:

- There is evidence for the simultaneous and collocated presence of mountain waves (MW) and non-orographic gravity waves (NOGW) during SOUTHTRAC flight ST08
- MW dominated above topography mainly over Tierra del Fuego and El Calafate and southeastwards whereas NOGW were predominantly identified above the oceans
- WRF performance with GW above very complex terrain has been tested against onboard-based observations up to the mesosphere

Corresponding author: Peter Alexander, peter@df.uba.ar

Abstract

We use observations from one of the SOUTHTRAC (Southern Hemisphere Transport, Dynamics, and Chemistry) Campaign flights in Patagonia and the Antarctic Peninsula during September 2019 to analyze possible sources of gravity wave (GW) in this hotspot during austral late winter and early spring. Data from two of the instruments onboard the German High Altitude and Long Range Research Aircraft (HALO) are employed: the Airborne Lidar for Middle Atmosphere research (ALIMA) and the Basic HALO Measurement and Sensor System (BAHAMAS). The former provides vertical temperature profiles along the trajectory while the latter gives the three components of velocity and temperature at the flight position. GW induced perturbations are obtained from these observations. We include numerical simulations from the Weather Research and Forecast (WRF) model to place a four-dimensional context for the GW observed during the flight and in order to present possible interpretations of the measurements, as for example the orientation or eventual propagation sense of the waves may not be inferred using only data obtained onboard. We first evaluate agreements and discrepancies between the model outcomes and the observations. This allowed us an assessment of the WRF performance in the generation, propagation and eventual dissipation of diverse types of GW through the troposphere, stratosphere and lower mesosphere. We then analyze the coexistence and interplay of mountain waves (MW) and non-orographic (NO) GW. The MW dominate above topographic areas and in direction of the so-called GW belt whereas the latter waves are mainly relevant above oceanic zones. WRF detects NOGW as mainly upward propagating entities above the lower stratosphere. Model runs show that deep vertical propagation conditions are in general favorable during this flight but also that in the upper stratosphere and lower mesosphere and mainly above topography there is some potential for wave breaking. The numerical simulations evaluate the GW drag for the whole flight area and find that the strongest effect is located in the zonal component around the stratopause. The general behavior against height resembles that obtained with ALIMA data. According to WRF results up to 100 km horizontal wavelength MW account for about half of the force opposing the circulation of the atmosphere.

1 Introduction

Gravity waves (GW) and the large scale planetary waves and tides are the main drivers for the general circulation of the middle atmosphere. The primary sources of GW are topography, convection, fronts, instabilities and spontaneous adjustment [e.g., Fritts and Alexan-

der, 2003]. GW constitute an important dynamical coupling mechanism between different regions and layers of the atmosphere by redistributing energy and momentum over large horizontal and vertical distances. They may transport both quantities away from the source area and release them in another zone during their dissipation. The deposition of momentum generates the GW drag which may accelerate, decelerate or sometimes even reverse the mean flow. An adequate representation of this drag in global circulation models is a key feature for realistic descriptions of the dynamical and thermal structure of the atmosphere. However, a significant part of the drag is due to small-scale GW and is not resolved by numerical models, which implies that their effect has to be parameterized through theoretical or observational means. Moreover, it has been shown that analysis or reanalysis data-sets cannot in general resolve GW horizontal wavelengths smaller than about 200 km [Preusse et al., 2014].

General circulation models usually produce in the middle atmosphere around 60^oS a too low GW drag [McLandress et al., 2012] during austral late winter and early spring. This leads in the stratosphere to stronger circumpolar winds and lower temperatures within the vortex than usually observed. Diverse causes have been suggested for the missing drag in the numerical models: large amplitude and short horizontal wavelength GW generated over the continental Andes and the Antarctic Peninsula and their downwind advection and meridional refraction into the polar night jet [e.g., Sato et al., 2012], mountain waves (MW) from small islands in the area which are not well-resolved by the numerical models [e.g., Hoffmann et al., 2016], secondary GW generated by the breaking of orographic waves [e.g., Satomura and Sato, 1999], GW related to winter storm tracks over the southern oceans [e.g., Hendricks et al., 2014; Plougonven et al., 2015] and spontaneous adjustment and instability around the polar night jet [e.g., Hindley et al., 2015; Geldenhuys et al., 2021].

The study by McLandress et al. [2012] showed that the models produced large zonal winds around 60^oS mainly located between 3 and 1 hPa. They also made numerical experiments with drag artificially added around that latitude and obtained more realistic stratospheric winds and temperatures. Garcia et al. [e.g., 2017] followed a similar procedure and also obtained improvements around the Antarctic polar vortex, and thereafter tested the effects of artificial non-orographic gravity waves (NOGW) which also led to better results. They therefore concluded that careful examination of observational evidence and model performance was required to establish which GW sources really produced the observed drag correction.

Most of the experiments and campaigns on GW in the lower and middle atmosphere usually focus on the Northern Hemisphere probably due to operational reasons. However, observations and model data indicate significant differences between both hemispheres. For example, a possible source of waves like the polar vortex is stronger and more persistent in the Southern Hemisphere. Global observations of GW exhibit several regions of large GW momentum flux around the globe. The region which seems to show the largest values encompasses the southern continental Andes and the Antarctic Peninsula [e.g., Ern et al., 2004, 2018]. The geographical area possesses steep topography and strong horizontal winds, which are favorable conditions to excite intense GW. Therefore the region attracted for over one decade several satellite and ground-based instrumentation studies [e.g., P. Alexander et al., 2010; de la Torre et al., 2012; Wright et al., 2016; Zhao et al., 2017; Llamedo et al., 2019; Kaifler et al., 2021; Reichert et al., 2021]. Another GW hotspot region may be found around New Zealand. The Deep Propagating Gravity Wave Experiment (DEEPWAVE) during the austral winter of 2014 was the first extensive observational campaign in the Southern Hemisphere devoted to the study of the generation, propagation and dissipation of GW [e.g., Fritts et al., 2016]. All these facts have been highlighting the research potential of a multi-platform study around the tip of South America.

The SOUTHTRAC (Southern Hemisphere Transport, Dynamics, and Chemistry) campaign took place in the hotspot around the Southern Andes and the Antarctic Peninsula during late austral winter and early spring in 2019 [Rapp et al., 2021]. The lidar system ALIMA (Airborne Lidar for Studying the Middle Atmosphere) flew for the first time on HALO (High Altitude and Long Range Research Aircraft). This is an upward-looking instrument which provides temperatures from approximately flight level (usually about 12 km) up to 80 km altitude [e.g., Kaifler et al., 2017]. The Basis HALO Measurement and Sensor System (BAHAMAS) recorded onboard high-frequency (100 Hz) in-situ measurements of position and the three components of atmospheric velocity, temperature and pressure [Giez et al., 2017, 2021]. The ST08 flight departed from Río Grande around 23 UTC on September 11, 2019 and landed in the same airport about 8 hours later. An initial analysis of the flight observations revealed a rich interplay of phenomena: the existence of large-amplitude GW, their deep upward propagation and breaking, the possible presence of secondary waves, refraction into the polar night jet and along the so-called GW belt and the superposition of wave modes [Rapp et al., 2021]. A later work by Kaifler et al. [2022] exhibited around topography a complex superposition of GW at various scales. The onboard cutting-edge instruments may

allow the unprecedented in-situ observation of details in a zone that hosts intense GW with a variety of possible origins not yet fully clarified.

Preliminary SOUTHTRAC results mentioned above show strong and complex GW activity hinting at the simultaneous presence of multiple sources. Below we try to locate and separate MW from NOGW and we intend to find some hints on the possible origin of the latter. We focus on some of the possible NOGW sources already mentioned above for the missing drag. Uccellini and Koch [1987] found that one possible source for inertia GW is the geostrophic adjustment associated with jet streaks. Plougonven et al. [2003]; Plougonven and Zhang [2014] mentioned significant inertia GW close to the jet axis and mainly around the maximum or the regions of strong curvature and concluded that they were due to geostrophic adjustment or in other words spontaneous emission. Or even the interaction of a jet with orography [Geldenhuys et al., 2021] or with MW [de la Torre et al., 2006] can lead to the excitation of GW. Therefore the polar night jet is a candidate for NOGW generation player, but not the only one. Cold fronts [Fritts and Alexander, 2003] and MW breaking due to convective or dynamic instability [Plougonven et al., 2008] are also possible mechanisms in this region.

This work should be considered complementary to de la Torre et al. [2022]. They use analysis data coincident with flight ST08 from a rotary spectral study perspective and compares them with observations whereas the present study uses an approach with mesoscale simulations. They also developed a classification of GW according to their orographic or non-orographic origin with the analysis data corresponding to the time and area covered by the airplane. In the troposphere and lower stratosphere above some zones, a net larger downwards energy flux was observed. As MW produce upward energy propagation, this indicates the possible relevance of NOGW in the studied region. As expected, the calculated upward GW energy flux rises close to mountains and also in some limited oceanic areas. Above the lower stratosphere the flux is much larger than below, providing evidence in the upper part for the presence of NOGW sources. Throughout the whole altitude interval there are upward and downward energy flows from possible MW and NOGW, with some departures from linear polarization and very complex patterns and interplay between both types of waves. In the present work we confirm some of these statements from the perspective of a mesoscale model and also find some discrepancies.

The simultaneous use of measurements and the Weather Research and Forecasting (WRF) numerical model may provide a fruitful combination of tools in order to unmask the complex combination of phenomena that may be present during the GW hotspot high-season. In particular, the numerical simulations may help to provide in the present work a spatial and temporal context of GW and their background around flight ST08 and may offer possible clues on the sources and evolution of the waves observed by onboard instruments. For example, information on the relative orientation between GW fronts and aircraft trajectory or real (not apparent as seen from HALO) horizontal wavelengths may be obtained from the model. Comparisons between onboard-based measurements and WRF may also allow a validation of the model and its settings over complex orography and up to the mesosphere.

In the second section we provide details about the data from the campaign instruments and from the numerical simulations performed for the flight and the tools for their processing. In the third section we review the atmospheric conditions before and during the flight. In the fourth section the mesoscale model becomes validated against the data from onboard instruments. The fifth section shows the results and their interpretation. Diagnostics based on linear and non-linear theory (polarization relations, links between energy and momentum fluxes, Richardson number, etc.) will be obtained with WRF data and will be used for a quantitative and qualitative analysis and interpretation of the scenario around the flight. It is our aim to disentangle the different contributions to GW activity observed during a flight with outstanding excitation and propagation conditions in order to possibly connect signatures and sources. Numerical simulations will be also used to assess the relative relevances of MW and NOGW in the drag along the flight path and over the whole area. The relative contributions to the drag of GW with short and long horizontal wavelength is also evaluated. In the final section we draw our conclusions.

2 Observations, simulations and data processing

2.1 Onboard instruments

ALIMA is an upward-pointing Rayleigh lidar system for airborne measurements using a pulsed neodymium-doped yttrium aluminum garnet laser transmitting 12.5 W at 532 nm with a 48-cm diameter receiving telescope, and using three height-cascaded elastic detector channels [e.g., Kaifler et al., 2017]. Optical filters inserted in the optical path in front of the photon detectors suppress the broadband solar background and thus allow for observations

in full daylight. An active beam stabilization system analyzes and corrects the alignment of the laser beams after each laser pulse, maintaining a precise lock of the beams to the field of view of the telescope even during aircraft maneuvers and occurrence of turbulence. Density is first obtained and then transformed into temperature using hydrostatic downward integration in the 20 to 90 km height interval. To isolate GW temperature oscillations a 30 min running mean (at typical flight speed it corresponds to about 420 km) is used as a representation of the background. The temporal resolution of 2 minutes (a rough aircraft displacement of 30 km) allows the detection of short horizontal wavelength GW, which supposedly make a significant contribution to the GW momentum flux. Profiles with 1 minute resolution may be also available with somewhat larger uncertainties.

The BAHAMAS measurement system consists of a nose tip probe setup on HALO with a 5-hole wind sensor and provides in situ measurements of both horizontal and vertical wind components as well as temperature and pressure and other physical quantities at flight altitude at a temporal resolution of 100 Hz [e.g., Giez et al., 2017]. Most SOUTHTRAC segments have been processed at 10 Hz as the corresponding horizontal scale is adequate for GW studies. The highest resolution data is usually used for turbulence analysis [e.g., Dörnbrack et al., 2022].

2.2 Numerical model settings

Numerical high-resolution simulations were performed with the 4.2 version of the WRF model [Skamarock and Klemp, 2008] forced with initial and boundary conditions from the National Centers for Environmental Prediction / Global Data Assimilation System (NCEP/GDAS) 0.25 x 0.25 degree global final analyses, which are provided every 6 hours. The data are available at 34 levels from 1000 to 1 hPa (roughly 42 km height). This solution was not used for any calculations or figures below unless otherwise stated. It just remained as a control simulation for tests in the coincident height interval against a run reaching the lower mesosphere as described in the next paragraph below. There were just minor discrepancies between both results. The application of WRF to a region with very sharp topography and to the simulation of the generation, propagation, and dissipation of the corresponding GW is a significant challenge. An adequate choice of numerical time step, horizontal and vertical resolution, physical parameterizations, domain locations and the tuning of diverse model coefficients becomes mandatory for a successful run. Three nested domains (d01, d02, d03) were used in the flight area at respectively 9, 3 and 1 km horizontal resolutions (see Fig-

ure 1). The three grid sizes are respectively (W-E x S-N) 364 x 382, 697 x 574 and 805 x 643. Figure 1 also shows the aircraft trajectory during flight ST08. The two largest computational domains fully contain the flight, whereas the smallest one is focused on a region with large amplitude MW. A Rayleigh damping layer was placed in the upper 10 km to attenuate GW reflection effects at the model lid (so simulations are affected by artificial diffusion from 32 to 42 km height). A time step of 36 s was chosen for the largest domain and scaled appropriately for the inner nests. The simulation started on September 11 at 00 UTC and ended 36 hours later. To allow for model spin-up, the simulations were used only 23 hours after the initial conditions. The physical parameterizations that were used are: microphysics (WSM 3-class simple ice scheme), short- and longwave radiation scheme (RRTMG), surface and boundary layer (Quasi-Normal Scale Elimination), land surface model (Unified Noah) and no cumulus scheme (it is assumed that the model is capable of producing it at the used resolutions). Model terrain height within domains was derived from the 30 s digital elevation model distributed with WRF. This was bilinearly interpolated onto the model grid. WRF outputs were provided every 6 minutes in order to adequately reproduce non-steady features and for comparison with high-resolution onboard measurements. This reference simulation has 90 vertical levels, whereby the coarsest resolution is around 600 m close to the model top at 1 hPa.

The inclusion of the stratosphere and mesosphere poses additional complications for the numerical model. We developed WRF simulations up to 0.01 hPa (roughly 75 km height) with ERA5 (fifth generation European Centre for Medium-Range Weather Forecasts atmospheric reanalysis) forcing data with 137 levels every hour and 0.30 x 0.30 degree horizontal resolution. Domains d01 and d02, their horizontal grid sizes and resolutions and physical parameterizations are the same as previously stated. Simulation start and spin-up interval are also repeated, whereby the run ended on September 12 at 07 UTC. A time step of 15 s was chosen for the largest domain and the damping sponge was placed in the upper 15 km. A shorter time step had to be now used to avoid numerical instabilities in the domain borders at high altitudes. The simulation possesses 150 vertical levels, whereby the coarsest resolution is 800 m close to the top. WRF outputs were provided every 15 minutes. Comparisons of the first and second runs in the 0 to 32 km height range lead to minor differences (not shown) providing a fair validation for an adequate functioning of deep WRF, at least in the lower half. The d02 files for the three components of velocity, temperature and pressure just for the

eight hours of the flight with 120 levels up to 60 km height occupy a space on disk of 150 GB.

The numerical simulations will be compared below against observations collected on board the HALO aircraft in order to validate WRF results. Model quantities from domains d02 and d03 were linearly interpolated in space and time to every HALO measurement. In Figure 1 we see the definition of the flight leg numbers. Each segment is essentially straight and stays at constant pressure with height changes within 500 m along several 100 km and no steep ascents, descents or turns. In this study we concentrated on legs 1, 2, 4 and 6. The first two segments are essentially diagonal flights in opposite direction over Southern Patagonia including the Andes, and the remaining two are nearly constant latitude trajectories with inverted sense above the Tierra del Fuego island area. These characteristics make these pairs of legs potentially comparable and in addition they cover a large fraction of the flight. In the figure we also show the location of Río Grande city, whose airport was used for departure and landing in all flights and El Calafate, whose surroundings are considered to be an intense MW hotspot.

2.3 GW interpretation tools

Oscillations of a GW happen in all three wind components as well as in density and pressure (and thus temperature) at the same frequency and three cartesian wavenumbers. There are magnitude and phase links between those quantities provided by the so-called polarization relations [e.g., Gill, 1982; Fritts and Alexander, 2003; Vadas, 2013] within linear theory. For the complex amplitudes $\tilde{u}$, $\tilde{v}$ of the zonal and meridional perturbation velocity components du and dv

$$\tilde{u} = \left(\frac{i\hat{\omega}k - fl}{i\hat{\omega}l + fk} \right) \tilde{v} \tag{1}$$

where $\hat{\omega}$, f refer to the wave intrinsic and inertial frequencies and k, l correspond to the zonal and meridional wave number components. From Eq. (1), in the general case an ellipse links both horizontal velocity amplitudes, whereby the eccentricity indicates the ratio of inertial to GW intrinsic frequency. In addition, the orientation of the major axis indicates the direction of horizontal phase propagation within an 180^{o} ambiguity. Scenarios like Andes where the typical wind speeds traversing the topography width define an intrinsic frequency range well below the inertial value lead to a simplified polarization relation

$$\tilde{u} = \frac{k}{l} \tilde{v} \tag{2}$$

so there is a nearly linear relation between both components and MW phase lags stay around 0 or 180 ^{o}. For example, Plougonven et al. [2008] used this polarization relation to study a MW over the Antarctic Peninsula. However, it should be recalled that certain orography can even generate inertia-GW [e.g., Queney, 1948; Dörnbrack et al., 2002].

For GW with a vertical wavelength smaller than about two density scale heights there is also a simple polarization relation between the complex amplitudes of the perturbations in temperature $\tilde{T}$ and vertical velocity $\tilde{w}$ as shown e.g. by Lu et al. [2015]

$$\tilde{T} = -\frac{iN^2}{g\hat{\omega}}\tilde{w}. \tag{3}$$

Here N and g are respectively the Brunt-Väisälä frequency and gravity and it is clear that both components stay in quadrature. These polarization relations will be used below in order to test the existence of GW in WRF or observational data and if they are present, then the expressions will be applied to scrutinize their possible source.

We will use the WRF domain d02 simulations in order to test the polarization relations and determine possible GW sources and distinguish between MW and NOGW. According to Eq. (2) high intrinsic frequency MW should exhibit a nearly linear relationship between the two horizontal velocity perturbation components. We set a range of 0^o or $180^o \pm 180^o/10$ phase difference range for them, whereby outside of this interval waves are considered to be eliptically polarized. In addition to this distinction, MW are required to exhibit vertical wavelengths between 5 and 20 km and NOGW between 2.5 and 5 km. This separation is justified by results shown below and by Ehard et al. [2015]; Reichert et al. [2021]. In addition, we require that MW signatures are present for at least one vertical wavelength and NOGW for four vertical wavelengths (at least four complete elliptical turns of the horizontal velocity perturbation should appear in a hodograph). We will use wavelet coherence along vertical columns above each grid point from the ground to 60 km height of u and v data to find the regions where both perturbation components very likely exhibit an associated behavior (magnitude-squared coherence larger than a given cutoff) at given times. This strict coherence cutoff is needed to have a clear identification of characteristic areas. Above every point of the grid the vertical wavelengths are determined from the wavelet scales and the height ranges for the existence of GW fingerprints are identified by the coherence staying above a given cutoff. Phase differences between both signals are found from the wavelet cross-spectrum. If at any geographical point there are two different GW types (MW and NOGW) at two different height intervals, then only the one with the strongest coherence is kept.

The phase difference between any two related signals is analyzed by wavelet coherence and cross spectrum [e.g., Torrence and Compo, 1998; Grinsted et al,, 2004]. The magnitude-squared wavelet coherence is a measure of localized correlation between two data series in the time-frequency or distance-wavenumber domains. This tool is useful for analyzing non-stationary or non-uniform signals and constrain the location of certain phenomena in time and frequency or distance and wavenumber planes. The coherence is computed here using the Morlet wavelet. The magnitude-squared wavelet coherence of two signals x_1 and x_2 with continuous wavelet transforms $W_1(a,b)$, and $W_2(a,b)$ at scale a and position b is given by

$$\frac{\mid S(W_1(a,b)^* W_2(a,b)) \mid^2}{S(\mid W_1(a,b) \mid^2) S(\mid W_2(a,b) \mid^2)}$$

whereby $*$ is complex conjugate and S is a smoothing operator in time (or distance) and scale which should be determined according to the observed coherence noisiness. The phase obtained from the wavelet cross-spectrum, which is a measure of the distribution of the power in the two signals, is employed to infer the relative lag between common modes in both data series. The expression for the wavelet cross spectrum at scale a and position b is

$$S(W_1(a,b)^* W_2(a,b)).$$

Notice that no filtering needs to be applied to the signals x_1 and x_2 as the wavelets are already doing the job of selecting the scales and comparing them.

3 Meteorological and dynamic conditions during flight ST08

The synoptic conditions during the flight time and region have been discussed by de la Torre et al. [2022] and are briefly recalled here. Dörnbrack et al. [2020] also discuss some meteorological aspects around El Calafate to the lee of Andes and within its area but a few hours before flight ST08. There was a low pressure level system near surface located to the East of the Antartic Peninsula on September 11, 18 UTC. It was associated to a cold front. The equivalent potential temperature gradient and the strong winds from SW at 850 hPA indicated the presence of incoming cold air above Southern Patagonia. A Pacific anticyclone around 55S carried polar air over the Drake passage. As a result, there was a strong low level wind blowing from SW over the Tierra del Fuego island, whereas a predominant westerly flow was present above Patagonia. Twelve hours later the Pacific anticyclone reached the continent while the low level pressure system and the front moved to the East. This resulted in a weakening of the low level wind over the land but kept similar intensity winds over the Drake passage. In Figure 2 we can see the mesoscale scenario for GW propagation ob-

tained from NCEP/GDAS 1 x 1 degree global final analyses. According to panels a-f, there is mainly a SW wind (angles between -180^o and -90^o) present at mountain altitudes in the region, with large values from the surface to the upper levels. This scenario provides optimal conditions for MW generation and deep propagation. Some irregular behavior in the angles at low heights is due to the presence of topography.

As a proxy for the jet as a possible source of NOGW, in panel g of Figure 2 we can see the horizontal wind magnitude and the location of the polar vortex edge, which was derived through the equivalent latitude of the largest potential vorticity gradient weighted by the horizontal wind speed [Nash et al., 1996] on September 11, 18 UTC and September 12, 00 and 06 UTC. ERA5 data have been used at 475K isentropic level (roughly 19 km height). The Southern polar vortex was displaced toward the tip of South America and broke down early during the late austral winter of 2019 due to a sudden stratospheric warming [Dörnbrack et al., 2020]. This restricted the propagation above 40 km height for MW in the hotspot area as from September 13th, while low-level conditions stayed optimal for their forcing. As a consequence, ST08 could have been the only flight of the campaign with excellent conditions for the deep propagation of MW in some segments, which may award it some unique characteristics.

4 Numerical model and comparison with measurements

In Figure 3 we show WRF cross sections from domain d02 along the four HALO flight legs respectively for vertical velocity w, temperature T and GW temperature perturbations dT. A horizontal 2D Fast Fourier transform filter was used for the latter. Modes are retained below a 500 km horizontal wavelength, whereby the limit is taken from preliminary campaign results showing the largest significant spatial periodicity observed. The GW isolation process was performed following the description by Kruse and Smith [2015]. Distance is reset to 0 at the start of every leg.

BAHAMAS and simulated quantities were compared at given flight times and positions (see Figure 4). Zonal and meridional velocity components u, v and T exhibit relations with slopes close to 1. However, w shows deviations from the identity line. Previous works based on observational data acquired during GW campaigns also found significant discrepancies between measured and simulated vertical velocity or associated quantities [e.g., Kruse et al., 2016; Wagner et al., 2017; Wildmann et al., 2021]. With the exception of some local

agreements, in general w fluctuations seem to occur on quite different scales and amplitudes. In the Appendix we made in domain d03 higher horizontal resolution (1 km) runs in legs 1 and 2 around Andes in order to find out if the departure between observed and WRF w is reduced, but no positive outcome was found. We also calculated in that section power spectral densities for w (PSD_w) for WRF and BAHAMAS values in two separate segments (with and without orography) in order to try to explain the different results from both data sources in the first and second half of leg 6 (see lowest left panel in Figure 5). Below we keep the use of WRF vertical velocity for the estimation of the GW drag force and the general identification of MW regions, but we will essentially apply phase lag conditions from polarization relations and vertical wavelength characteristics to both horizontal velocity components of the model to better identify possible GW sources.

Model and BAHAMAS w, T and dT in the flight position and time along four flight segments are shown in Figure 5. Temperature perturbations are filtered along HALO distance and therefore represent onboard apparent modes (it is not possible to infer based only on BAHAMAS data or any onboard measurements the relative orientation between wave fronts and airplane trajectory). The cutoff in this case was set to 800 km to account for the fact that in general the airplane legs may not be perpendicular to the GW fronts and so apparent horizontal wavelengths may be larger than real ones. The average flight speed was around 850 km/h and in addition we considered the mean between the WRF resolution when the aircraft moves along meridians or parallels (3 km) and a bisector (4.2 km). Observational data have been averaged over 15 s in order to make the horizontal resolution of observational and numerical values comparable. Model results and observations clearly exhibit larger GW activity above and to the East of topography in Figures 3 and 5. The closest match of w, T and dT between WRF and BAHAMAS may be observed in the first 400 km of leg 6 in coincidence with modest height and slightly sloped topography. For brevity the horizontal components u, du, v and dv are omitted but the general agreement between WRF and BAHAMAS resembles T and dT.

Numerical simulations have been horizontally averaged over 30 km to establish comparisons with ALIMA data (the lidar profiles are obtained over 2 minutes), whereas these values are shown below in the coincident 20-60 km height range. The instrument was affected at some times and altitudes by the presence of polar stratospheric clouds or other issues also impeding the adequate derivation of temperature. Figures 6 and 7 show respectively the comparisons of T and dT filtered between 2 and 20 km of vertical distance [e.g.,

Ehard et al., 2015; Kaifler et al., 2020]. To ensure that the largest vertical wavelengths do not include significant contributions from planetary waves we plotted the same as Figure 7 but for the perturbations in the spectral range 15 to 20 km for WRF and ALIMA (not shown) and noticed no horizontal structures of several 100 km with the exception to the West of Andes in leg 1. In this instance vertical filtering is selected as from the ALIMA perspective the relative orientation of wave fronts and aircraft trajectory is unknown. This procedure seems to be physically more adequate if only onboard data are employed as the horizontal wavelength cutoffs chosen along a flight path may be somehow arbitrary without information on the angle between the horizontal wave vector and airplane path. For example, a finite horizontal wavelength can become apparently infinite as detected onboard if the airplane is by chance flying parallel to a constant phase line [e.g., de la Torre et al., 2018]. Measured values will always be equal or larger than the real ones. In Figure 6 we notice that although both data sources have very different nature they show a coherent picture from the troposphere up to the mesosphere along the four flight legs. The stratopause is observed around 50 km height in both cases. Quantitatively, the observational perturbation amplitudes in Figure 7 differ from WRF solutions but there is a qualitative agreement in order of magnitude and general trends. A significant change in GW behavior is observed around 40-45 km height in some segments and deep propagation in others. We see the MW to the East of Andes in legs 1 and 2 with large amplitudes in dT. Legs 3 and 4 also exhibit intense MW, mainly close to topography. In Figure 7 there is a superposition of GW of different scales but it is difficult for the eye to distinguish all of them. Kaifler et al. [2022] studied diverse spectral bands in order to separate different GW modes present during ST08.

5 Results for ST08

5.1 Identification and analysis of GW types

We start with some warnings on the complexity of the integration of a large number of data from diverse sources, their processing and physical interpretation. These subjects have already been addressed in previous publications so we do not go into details but we would like to enumerate them as they are a key issue in the use of the campaign results. First we recall that there is no unique way of separating in the observations the GW from the background, tides, planetary waves or noise and diverse methods may lead to different results [e.g., John and Kumar, 2013; Ehard et al., 2015]. Moreover, it will be noticed that it is not possible to keep the same filtering process for all the data in the present work, as different

sources have diverse horizontal and vertical resolutions and may have a one- , two- or three-dimensional perspective. This leads to different minimum or maximum wavelength cutoffs or filtering in the horizontal or the vertical directions for optimization. Second, every instrument may be observing GW in a different spectral range and height and may be operative under different weather conditions [e.g., Preusse et al., 2009]. Third, as measurements are not performed simultaneously in the three space dimensions and time, the inferred wavelengths or periods are apparent and usually differ from the real ones [e.g., P. Alexander and de la Torre, 2010; de la Torre et al., 2018]. Careful interpretation is necessary. Fourth, we are submerged in a difficult scenario with no ideal monochromatic waves but rather packages, groups or superpositions of them or may be there is a dominant mode accompanied by other ones and in addition the linear regime assumption may be fragile.

In videos 1 and 2 in the supplement we show the evolution according to WRF domain d02 of w and dT every 15 min during the flight at 10, 30 and 55 km height (roughly at the tropopause, stratosphere and mesosphere). In both quantities it can be seen that the largest GW activity occurred in the first few hours of the flight, mainly above continental Andes and Tierra del Fuego island with amplitudes generally increasing significantly with height. It is predicted by linear theory that the vertical velocity is significant for high intrinsic frequency MW, whereas the horizontal components or temperature may be better suited for the identification of the opposite part of the spectrum [e.g., Gill, 1982]. By comparing the videos it can be seen that the vertical velocity exhibits a more localized pattern above the Andes, confirming that it is a good predictor of MW. It also can be seen that the most significant amplitudes correspond to horizontal wavelengths not much larger than about 100 km. In Figure 8 we see for WRF domain d02 a horizontal cross section at 15 km height for w and dT with a horizontal filter cutoff of 500 km on September 12 at 00 UTC. Signatures of prolongation into the so-called GW belt are clearly seen. The flow over Andes generates the MW that extend downwind and poleward. The two main sources seem to be El Calafate and Tierra del Fuego island areas.

In Figure 9 we show the results of the GW type identification method explained in section 2.3 on September 12 at 00, 02, 04 and 06 UTC. The flight path and the aircraft position at the evaluated times are also exhibited. MW generation at the El Calafate and Tierra del Fuego areas and their advection towards SE are clear during the whole sounding. In addition, NOGW signals are present in the Drake Passage and surrounding area, mainly above oceanic sectors. This fact coincides with many aspects of the rotary spectral study on analysis data

during ST08 by de la Torre et al. [2022]. The presence of NOGW over the oceans in this region has already been highlighted by Hertzog et al. [2008]; Plougonven et al. [2013]. These aspects resemble results from the DEEPWAVE campaign where MW were mainly found over Tasmania and the South Island and NOGW across the Southern Ocean [Eckermann et al., 2019]. The MW over the Southwest at 02 UTC in Figure 9 are of unknown origin or an error of the method. Their approximate vertical localization and wavelength are respectively 20 to 60 km and 17 km whereby the phase difference is about 10^o. Taking into account the HALO position over time it is clear that MW should have been detected by onboard instruments over the 4 analyzed legs but mainly above the 2 first ones, whereas NOGW might have been present over the second half of leg 2 and the first half of leg 4. In general, the flight rather traversed MW than NOGW. MW sources were apparently dimming by the end of the flight but the wave drift from Andes towards the belt could still be seen (see videos 1 and 2). Although it is not shown in Figure 9, in each vertical column where the coherence for a mode stayed above 0.9 we determined the altitude of local maximum coherence and the surrounding interval that was still above that cutoff. This allowed us to estimate with the mode vertical wavelength the number of clearly detectable turns and verify the requirements for MW and NOGW. The figure should not be understood as an exact identification of the location of diverse types of waves but rather in terms of rough areas with likelihood for the presence of them. For example, in Figures 3, 5, 7 and 8 it is clear that when HALO was about the Andes in legs 1 and 2 it crossed strong MW. In Figure 9 just some dots identifying MW are close to those flight positions and times. However, if we look at the overall picture we will realize that this part of the airplane trajectory is embedded in a clearly (green) MW dominated region of several 100 km in both cardinal directions. From a general overview of the figure there is a clear potential for the coexistence in the whole area of MW and NOGW. For example, when analyzing the upper panel on the left of Figure 9 there is a clear dominance of NOGW from the South Pacific into partially the Atlantic Ocean and also to the Northeast of the Malvinas Islands. And there is a supremacy of MW in the continent, at the North of Tierra del Fuego and towards the East and Southeast directions. Finally, to the East of the large island both types of GW may likely coexist.

Next we use BAHAMAS data for comparison with these findings and first focus on wavelet magnitude-squared coherence above 0.7 for w and T for apparent horizontal wavelengths larger than 24 km as seen from the aircraft trajectory. The chosen wavelength lower cutoff is somehow arbitrary with respect to the expected lowest horizontal distance between

fronts as seen by the possibly slant path of HALO in the wave field (as explained above horizontal wavelengths measured from the airplane will be larger than real ones). Both magnitudes should be nearly in quadrature for GW unless the vertical wavelength is roughly larger than two atmospheric scale heights according to Eq. (3). In Figure 10 we show these results, including the phase difference departure from ideal 90^o at the location of maximal correspondence between both quantities. Values above 18^o could be considered non-GW structures or large vertical wavelengths. A variety of GW seems to be present in all legs mostly at shorter apparent horizontal wavelengths. From the coherence analysis of both horizontal velocity perturbations in Figure 11 we notice that the phase difference departure below 18^o from ideal linear polarization 0^o or 180^o indicates that MW may be present along the 4 studied legs. NOGW may be present in the final part of leg 2 and in the initial section of leg 4 (phase difference above 18^o and apparent horizontal wavelength above 100 km). Notice that also with BAHAMAS data NOGW are mainly detected above the ocean. Our 100 km lower limit is somehow arbitrary but reflects the fact that NOGW as short as some MW are less likely to be found (see below Figure 18). Figures 10 and 11 are not fully consistent and therefore need some further discussion on some discrepancies. For example from Figure 10 one would expect short apparent horizontal wavelength MW in legs 1 and 2 above the mountains. However, they are not observed in Figure 11. One possible cause is that the simple polarization relation in Eq. (2) may not hold at some instances because at least one of the assumptions departs from the stated conditions. This might also explain why in Figure 9 the same area is not so full of MW (green) dots. We should recall here that the BAHAMAS results refer exclusively to what becomes detectable at flight altitude.

From the results in the two previous paragraphs we concentrate our search for NOGW in legs 2 and 4 and try to determine some of their general characteristics. We study the coherence of both horizontal velocity perturbation components from WRF along the two flight segments in the vertical columns 0 to 60 km every 30 km of aircraft displacement. We evaluate the phase difference at the height of maximal coherence and wherever it exceeds 0.7 we determine the altitude interval around that position where it stays above that value. Nearly all possible NOGW detected in terms of phase difference and a minimum of 4 turns stayed within 2.5 to 5 km vertical wavelength (Figure 12), which justifies our above cutoff of 5 km between NOGW and MW. Regions favorable to the presence of NOGW should be recognized by the repeated exhibition of large columns of high coherence and angles that depart more than 18^o from the linear MW ideal condition. In agreement with above findings we no-

tice in Figure 12 that the presence of NOGW is corroborated away from sharp topography in leg 2. Along leg 4 (above the ocean) we see the identification of NOGW with a few void intermittencies. This type of wave is essentially visible in WRF above 20 km height. Figure 9 suggested that this is a region of encounter between the MW belt and NOGW. Restricting our analysis for that figure to only NOGW and separating them into clockwise and counterclockwise turns with increasing height (respectively downward and upward energy in the Southern Hemisphere) we notice an overwhelming majority of the latter ones in Figure 13. We may conclude that WRF mainly detects NOGW propagating upwards. Either the numerical model is not able to generate downwards propagating NOGW or the physical source mainly generates them in the opposite direction. In agreement with WRF preference of NOGW above the sea, Geldenhuys et al. [2022] detected roughly between 30 and 50 km height with a ray tracer on September 11 at 14 UTC possible evidence of NOGW generated by the jet over the Pacific Ocean upwind of the Andes.

In order to further analyze NOGW in the region we study them in the Drake Passage area where according to Figure 9 they exhibit a significant presence at least in the initial hours of September 12. In Figure 14 we show the perturbed horizontal velocity components around the flight area at 25 km height on September 12, 02 UTC according to WRF. Although vertical wavelengths of the three-dimensional profiles have been filtered between 2.5 and 5 km, it is clear that it is not possible to fully eliminate some fingerprints of MW that possess short horizontal scales (the alternating fringes): in the Southeast zone of the panels a region with homogeneous sectors (large horizontal scale NOGW) but also with weak fronts (presumably traces of MW after filtering) may be seen. In Figure 15 we observe the NOGW in this area with zonal and meridional vertical cross sections of both horizontal velocity perturbations (in the position of the cross in the upper panel of Figure 14). Every ^{o} represents here in latitude and longitude respectively about 111 and 60 km. Fronts are more clearly visible above 25 km height. Vertical wavelengths generally stay around 5 km. In Figure 16 we see the rotation of the horizontal perturbation vector in the position of the asterisk in the upper panel of Figure 14 (this point was chosen for the clean rotation as compared to other ones in the Drake Passage). About six full cycles happen in the height interval from 26 km to 56 km (vertical wavelength around 5 km). The ellipse orientation seems to show that the wave vector direction is mainly West to East (with an ambiguity of 180^o). The eccentricity in general is not larger than 1/2. Its slight change with height (i.e. of the intrinsic wave frequency) may be only explained by the fact that we have no monochromatic mode but rather a packet.

In the complementary work [de la Torre et al., 2022] it is shown through a spectral analysis in the flight area and time of ST08 that monochromatic waves are hardly found and rather bands around one or two dominant modes are detected.

It is noteworthy that most NOGW observed by WRF (Figures 12, 15 and 16) are located above the lower stratosphere (see Figure 3), propagating upwards and usually around regions dominated by MW. We therefore evaluate the Richardson number (Ri) values in order to probe another possible NOGW source like MW breaking due to convective or dynamic instability by respectively verifying values below 0.25. It is calculated as

$$\mathrm{Ri} = \frac{N^2}{(dU/dz)^2}$$

where $(dU/dz)^2$ refers to the squared vertical gradient of both horizontal velocity components and $N^2 = g/\theta\ \partial\theta/\partial z$ with θ potential temperature. The so-called wave-modulated or local Richardson number [Nappo, 2012] has been here calculated. We therefore set the filter cutoffs selectively to the vertical profiles. Scales shorter than 20 km are removed for the potential temperature θ (it now represents the background) whereas only the ones smaller than 5 km are eliminated for its vertical derivative $\partial\theta/\partial z$ (it then corresponds to the gradient of the large scale with GW perturbations). The wavelengths shorter than 5 km become removed for the horizontal wind components. A few notable zones emerge along the four segments from the condition Ri < 0.25 and are shown in green in Figure 7. They are mainly located over Andes in leg 1 and always above 45 km. The marked areas are in agreement with the above description of ALIMA and WRF data showing a notable change in GW behavior in the upper stratosphere in some segments. The features may be interpreted as GW breaking or attenuation and secondary waves around that height. However, considering this altitude, the phenomenon cannot be the source of all the NOGW that are mainly above the oceans. Then, there is a chance that some of these waves are the leftovers from the cold front mentioned above as it agrees with the WRF result of nearly all those waves propagating upwards.

We also use the Scorer parameter [Scorer, 1949]

$$L^2 = \frac{N^2}{U^2} - \frac{1}{U}\frac{d^2U}{dz^2}$$

in order to distinguish areas where MW, if they are present, may be evanescent, trapped or vertically propagating. According to the parameter definition N and U are the corresponding background profiles. The calculations lead to permitted horizontal wavelengths above a few km except in some areas represented as yellow in Figure 7, where the Scorer parameter

becomes negative and no MW could propagate conservatively upwards. This is contrary to a sometimes made assumption that the first term in the Scorer parameter definition may be dominant. At least from the present simulations this may not be the true behavior in some parts of the mesosphere. This situation seems to occur above the mountains around 50 km height in the first two legs (with some amplitude attenuation above them) and around 60 km in the last two ones. Finally, it is interesting to notice that after an analysis above legs 1 and 2 with a Fourier ray model Kaifler et al. [2022] also find that there is potential for wave breaking in the upper stratosphere and lower mesosphere over the mountains.

5.2 GW energy, momentum flux and drag

We now calculate GW energy and zonal and meridional momentum fluxes (EF, MF_x, MF_y) at flight level as indicated by Smith et al. [2008, 2016] and compare between results obtained with BAHAMAS and WRF data. Averages per segment are calculated as

$$\begin{aligned} MF_x &= \frac{\overline{\rho}}{S}\int dudwdS \\ MF_y &= \frac{\overline{\rho}}{S}\int dvdwdS \\ EF &= \frac{1}{S}\int dpdwdS \end{aligned}$$

from GW perturbations in the three components of velocity du, dv, dw and pressure dp, $\overline{\rho}$ is the average density over the segment and S and dS are its length and a differential displacement over it. According to Eliassen and Palm [1960] for linear, steady, small-amplitude, non-dissipative MW

$$-EF = \overline{u}MF_x + \overline{v}MF_y$$

with zonal and meridional velocities $\overline{u}$ and $\overline{v}$ averaged per leg. Perturbations are obtained by removing any mean and linear trend along the segment. A hydrostatic correction is previously applied to pressure. Departures from the above relation may indicate deviations from the cited assumptions. In our case with the exception of leg 1 we cannot claim that most observed GW are MW. In addition, with respect to above results, we cannot assume that all perturbations are linear, steady, small and non-dissipative. However, the relation is here roughly obeyed. Values are within usual ranges and they approximately agree with calculations from Dörnbrack et al. [2022], who analyzed 357 segments of the whole SOUTHTRAC campaign. Their legs 1, 2, 4 and 5 are similar but not coincident with our 1, 2, 4 and 6. In Table 1 we compare our values obtained from BAHAMAS and WRF. Notice that almost all values are positive, which implies possible upward propagating MW carrying negative momentum.

We mention that when we filtered out from BAHAMAS any fluctuations over an interval smaller than 150 consecutive data (15 s, which is roughly equivalent to a HALO distance of 3 km) in order to mimic the WRF horizontal resolution, then the results did not change significantly so we omit them here. Leg 4 exhibits consolidate differences between EF and $-(\overline{u}MF_x + \overline{v}MF_y)$ within WRF and BAHAMAS data and this could be attributed that it is fully above ocean and according to our above results more susceptible to the presence of NOGW. The only negative value (Leg 2 with BAHAMAS data) could be attributed to its long raid over the ocean (where a significant amount of NOGW may be present according to Figure 9). This large negative value in the same leg was also found by Dörnbrack et al. [2022]. However, $EF < 0$ has previously also been obtained in some MW dominated areas with no unique explanation [e.g., Smith et al., 2008; Wagner et al., 2017; Dörnbrack et al., 2022].

GW momentum flux was calculated from the WRF simulation in a rectangle containing the whole flight area and the corresponding drag zonal and meridional components were obtained for horizontal wavelengths shorter than 500 km (Figure 17), as explained by Kruse et al. [2016]. The two drag projections had comparable negative components but the zonal contribution was generally larger. There is one order of magnitude increase about 25 km height and a maximum at 50 km altitude. GW horizontal refraction caused by wind gradient may be one of the contributors to the drag due to the variations it produces on momentum flux [Geldenhuys et al., 2022]. In coincidence with the GW activity exhibited by both videos, the largest intensity occurs at the beginning of the flight and thereafter there is a weakening evolution. The drag values and profiles are similar to those calculated by other means in this GW hotspot area [Kaifler et al., 2020]. By neglecting the contribution from GW close to the inertial frequency as the factor $F = 1 - f^2/\hat{\omega}^2$ tends to 0 for those waves [Fritts and Alexander, 2003] and assuming a linear regime we obtained the zonal drag as

$$-\frac{1}{\bar{\rho}}\frac{d}{dz}(\bar{\rho}\overline{dudw}) \tag{4}$$

where $\bar{\rho}$ here represents the background density, z the altitude, $\overline{dudw}$ the Reynolds stress averaged over at least one typical horizontal wavelength distance or area (a similar expression holds for the meridional drag). We should assess the uncertainty introduced in the calculation by assigning to F a value of 1 also to the GW that stay away from the high intrinsic frequency regime, at least at altitudes where the drag is large (above 25 km). From Figure 16 we may derive representative information. The eccentricity of the ellipse indicates the ratio of wave intrinsic frequency to Coriolis parameter $f/\hat{\omega}$. Above 25 km the value is about 1/2

or even lower. This implies that the contributions from NOGW to the total drag could be at most 25% lower than when we use an F value of 1.

The strongest drag components may be observed in the upper panels of Figure 17 around the upper stratosphere and stratopause, and it coincides with the altitudes mentioned by McLandress et al. [2012] for the missing drag. Above 40 km height there is a trend towards a sign reversion of the force. In the lower panels of the figure we recalculate the drag but only for horizontal wavelengths smaller than 100 km. They explain a very large portion of the total drag above 25 km height, mainly close to the stratopause. Figure 15 give an idea of ranges of NOGW horizontal wavelengths. A sharp spectral separation from MW may in general not be possible. In Figure 18 we show the power spectral density for both horizontal velocity components at three different heights for respectively regions dominated by MW and NOGW according to Figure 9 on September 12, 00 UTC (roughly longitude -75 to -65^o and latitude -55^o to -47^o and longitude -85^o to -75^o and latitude -50^o to -58^o). It may be noticed that in general MW dominate the spectrum (keep in mind that PSD scales are logarithmic) at total horizontal wavelengths lower than 100 km. We may therefore evaluate that most of the drag from this spectral range stems from MW, which is roughly half the total opposing force at those heights.

From the above comments on the discrepancy of w between WRF and BAHAMAS at flight level it is clear that the current drag results are disputable. However, we remark the notable similarity of our results with the drag profiles from Kaifler et al. [2020] obtained with a lidar in the same region and season of the year. Kaifler et al. [2022] independently from WRF obtained the drag components from ALIMA measurements along legs 1 and 2 in flight ST08. There are some similarities and some discrepancies with our WRF results. We both find that negative components prevail with local peaks at 35-40 km and 50-55 km height. A sign reversion is seen around 45 km in both works. However, Kaifler et al. [2022] observe the same behavior at 35 km and we do not. We obtain a rough equipartition between short and large horizontal wavelengths (separation around 100 km) and they see a much more significant contribution from the small scales. Our drag intensity is generally smaller than theirs. It should be considered that drag determinations in both studies use different data sources (ALIMA and a Fourier ray model vs WRF) and formulas: see above our Eq. (4) and compare with the expression from Ern et al. [2017] that they applied. Even different filtering procedures are used. In addition, detailed agreement is not expected as we evaluated the values over the whole flight area and time and they did it individually over legs 1 and 2 at

657 the time and position where HALO was present. And they used four horizontal wavelength
658 intervals for some parts of their analysis and we considered just two.

659 6 Conclusions

660 From the numerical simulations we may infer that the most intense GW occurred be-
661 fore and at early flight stages of flight ST08. They were located above Andes with ampli-
662 tudes increasing significantly with height. The cleanest GW vertical patterns in the WRF
663 mesoscale simulations may be found in leg 1 above Andes. The two main local sources of
664 MW from the numerical simulations are El Calafate and Tierra del Fuego. These waves ex-
665 tend southeastwards towards the so-called GW belt. WRF and BAHAMAS both indicate
666 the presence of significant NOGW above the ocean but no clear source could be identified.
667 This configuration of MW mainly above topography and NOGW above the ocean has also
668 been observed in another hotspot during the DEEPWAVE campaign. The classification of
669 waves into MW or NOGW has been done using WRF and BAHAMAS data with polariza-
670 tion relations and by verifying links between energy and momentum fluxes. According to
671 Figure 9, flight ST08 mainly probed MW rather than NOGW. The calculation of Richardson
672 and Scorer numbers shows some localized places in the four studied legs, mainly above the
673 mountains, where GW in the upper stratosphere or lower mesosphere may undergo instabil-
674 ity.

675 Some results of the rotary spectral study on analysis data by de la Torre et al. [2022]
676 and some outcomes of our work based on mesoscale simulations in the region and time of
677 flight ST08 should be highlighted together. Their calculated upward GW energy flux is gen-
678 erally largest around the mountain zones and in some oceanic areas. They found that above
679 the lower stratosphere the energy fluxes are much larger than below. Throughout the whole
680 altitude interval there are upward and downward flows from possible MW and NOGW, with
681 some departures from linear polarization and presence of both types of waves. We found
682 with WRF linearly polarized GW mainly over Andes and towards Southeast. NOGW were
683 essentially detected over oceans and propagating upwards above the lower stratosphere. A
684 possible coexistence of both types of waves was noticed around the Drake Passage.

685 The performance of WRF with GW above very complex terrain has been tested against
686 onboard-based observations up to the mesosphere. T, u and v behaviors are well reproduced.
687 There is not such a good agreement in w between WRF and BAHAMAS but in a few no-

table cases. This is no surprise in relation to previous works. WRF and ALIMA show corresponding general features in T between 20 and 60 km, whereas dT patterns are similar but sometimes differ in the amplitudes. The WRF and ALIMA outcomes show signatures of GW breaking and dissipation or secondary wave excitation at some nearly coincident stratospheric or mesospheric levels close to mountains and deep propagation in other parts. The drag produced above the whole studied area during the flight by WRF had comparable zonal and meridional negative components and they were in general accordance to ALIMA profiles close to Andes. The WRF drag general outlook (order of magnitude, sign, increasing and decreasing vertical intervals) also resembles the seasonal profile obtained by a fixed lidar in this geographical region [Kaifler et al., 2020]. There is a significant GW drag rise from WRF about 25 km height with a maximum around 50 km height, mainly at the beginning of the flight. Thereafter the values became less intense. About half of the drag may be attributed to the horizontal wavelengths shorter than 100 km (more likely MW than NOGW) according to WRF.

7 Appendix

In the aim of testing wether a higher horizontal resolution of WRF leads to a closer agreement between observed and modeled vertical velocity we show results within domain d03 for one segment of leg 1 and another one from leg 2 which are mainly around Andes (Figure A1). The model was forced with NCEP/GDAS data. No approach between both data sources may be noticed in these additional results (compare with Figures 4 and 5).

From Figure 5 we may also conclude on w that in the analyzed scenario WRF seems to display essentially the effects of flow perturbations due to topography. Away from orography the discrepancies are quite clear across a broad range of scales, but mainly among the smallest ones. These facts become clear when plotting PSD_w for WRF and BAHAMAS after dividing leg 6 into 2 halves, the first one above and close to topography and the second one over the ocean (Figure A2). Notice also that domain d02 model data are meaningless above wave number 0.17 1/km as the horizontal resolution is 3 km, whereas BAHAMAS results show no abrupt behavior change there.

Acknowledgments

Manuscript prepared under grants CONICET PIP 2017-2019 11220170100067CO and ANPCYT PICT-2018-00653. P. Alexander, A. de la Torre, P. Llamedo and R. Hierro are members of

719 CONICET. The computational resources used in this work were provided by the HPC center
720 DIRAC, funded by Instituto de Física de Buenos Aires (UBA-CONICET) and by SNCAD-
721 MinCyT initiative. Assistance from DIRAC staff is also greatly appreciated. ERA5 profiles
722 were downloaded from https://cds.climate.copernicus.eu whereas NCEP/GDAS data were
723 obtained from https://rda.ucar.edu. The indications by C. Kruse for successfully running
724 deep WRF are very much appreciated.

725 References

726 Alexander, P. and de la Torre, A. (2010), A Method to Infer the Three Cartesian Wavelengths
727 of a Mountain Wave from Three Soundings, *J. Appl. Meteor. Climatol.*, *49*, 2069–2074,
728 doi:10.1175/2010JAMC2348.1.

729 Alexander, P., Luna, D., Llamedo, P., and de la Torre, A. (2010), A gravity waves study close
730 to the Andes mountains in Patagonia and Antarctica with GPS radio occultation observa-
731 tions, *Ann. Geophys*, *28*, 587–595.

732 de la Torre, A., Alexander, P., Llamedo, P., Menèndez, C., Schmidt, T., and Wickert, J.
733 (2006), Gravity waves above the Andes detected from GPS radio occultation temperature
734 profiles: Jet mechanism?, *Geophys. Res. Lett.*, *33*, L24810, doi:10.1029/2006GL027343.

735 de la Torre, A., Alexander, P., Hierro, R., Llamedo, P., Rolla, A., Schmidt, T., and Wickert, J.
736 (2012), Large-amplitude gravity waves above the southern Andes, the Drake Passage, and
737 the Antarctic Peninsula, *J. Geophys. Res.*, *117*, D02106, doi:10.1029/2011JD016377.

738 de la Torre, A., Alexander, P., Schmidt, T., Llamedo, P., Hierro, R. (2018), On the distortions
739 in calculated GW parameters during slanted atmospheric soundings, *Atmos. Meas. Tech.*,
740 *11*, 1363–1375, doi:10.5194/amt-11-1363-2018.

741 de la Torre et al.(2022). Submitted to the same special issue. A spectral rotary analysis of
742 gravity waves: An application to a SouthTRAC-GW research flight.

743 Doörnbrack, A., T. Birner, A. Fix, H. Flentje, A. Meister, H. Schmid, E. V. Browell, and M.
744 J. Mahoney (2002), Evidence for inertia gravity waves forming polar stratospheric clouds
745 over Scandinavia, *J. Geophys. Res.*, *107*, 8287, doi:10.1029/2001JD000452.

746 Dörnbrack, A., Kaifler, B., Kaifler, N., Rapp, M., Wildmann, N., Garhammer, M., Ohlmann,
747 K., Payne, J.M., Sandercock, M. and Austin, E.J. (2020), Unusual appearance of mother-
748 of-pearl clouds above El Calafate, Argentina (50^o21S, 72^o16W), *Weather*, *75*, 378–388,
749 doi:10.1002/wea.3863.

Dörnbrack et al.(2022). To be submitted to the same special issue. High-resolution aircraft observations of turbulence and waves in the free atmosphere and comparison with global model predictions.

Eckermann, S. D., Doyle, J. D., Reinecke, P. A., Reynolds, C. A., Smith, R. B., Fritts, D. C., and Dörnbrack, A. (2019), Stratospheric Gravity Wave Products from Satellite Infrared Nadir Radiances in the Planning, Execution, and Validation of Aircraft Measurements during DEEPWAVE, *J. Appl. Meteor. Climatol.*, *58*, 2049–2075, doi:10.1175/JAMC-D-19-0015.1.

Ehard, B., Kaifler, B., Kaifler, N., and Rapp, M. (2015), Evaluation of methods for gravity wave extraction from middle-atmospheric lidar temperature measurements, *Atmos. Meas. Tech.*, *8*, 4645–4655, doi:10.5194/amt-8-4645-2015.

Eliassen, A. and Palm, E. (1960), On the transfer of energy in stationary mountain waves, *Geofys. Publ.*, *22*, 1–23.

Ern, M., Preusse, P., Alexander, M.J., and Warner, C.D. (2004), Absolute values of gravity wave momentum flux derived from satellite data, *J. Geophys. Res.*, *109*, D20103, doi:10.1029/2004JD004752.

Ern, M., Hoffmann, L., and Preusse, P. (2017), Directional gravity wave momentum fluxes in the stratosphere derived from high-resolution AIRS temperature data, *Geophys. Res. Lett.*, *44*, 475–485, doi:10.1002/2016GL072007.

Ern, M., Trinh, Q. T., Preusse, P., Gille, J. C., Mlynczak, M. G., Russell III, J. M., and Riese, M. (2018), GRACILE: a comprehensive climatology of atmospheric gravity wave parameters based on satellite limb soundings, *Earth Syst. Sci. Data*, *10*, 857–892, doi:10.5194/essd-10-857-2018.

Fritts, D.C. and J. Alexander (2003), Gravity wave dynamics and effects in the middle atmosphere, *Rev. Geophys.*, *41*, 1003, doi:10.1029/2001RG000106.

Fritts, D.C., R.B. Smith, M.J. Taylor, J.D. Doyle, S.D. Eckermann, A. Dörnbrack, M. Rapp et al. (2016), The Deep Propagating Gravity Wave Experiment (DEEPWAVE): An Airborne and Ground-Based Exploration of Gravity Wave Propagation and Effects from Their Sources throughout the Lower and Middle Atmosphere, *Bull. Amer. Meteor. Soc.*, *97*, 425–453, doi:10.1175/BAMS-D-14-00269.1.

Garcia, R. R., Smith, A. K., Kinnison, D. E., de la Cámara, A., and Murphy, D. J. (2017), Modification of the Gravity Wave Parameterization in the Whole Atmosphere Community Climate Model: Motivation and Results, *J. Atmos. Sci.*, *74*, 275–291, doi:10.1175/JAS-D-

16-0104.1.

Geldenhuys, M., Preusse, P., Krisch, I., Zülicke, C., Ungermann, J., Ern, M., Friedl-Vallon, F., and Riese, M. (2021), Orographically induced spontaneous imbalance within the jet causing a large-scale gravity wave event, *Atmos. Chem. Phys.*, *21*, 10393–10412, doi:10.5194/acp-21-10393-2021.

Geldenhuys et al.(2022). Submitted to the same special issue. Observations of gravity wave refraction and its causes and consequences, doi: 10.1002/essoar.10511036.1.

Giez, A., C. Mallaun, M. Zöger, A. Dörnbrack, and U. Schumann (2017), Static pressure from aircraft trailing-cone measurements and numerical weather prediction analysis. *J. Aircr.*, *54*, 1728–1737, doi:10.2514/1.C034084.

Giez, A., C. Mallaun, V. Nenakhov and M. Zöger (2021), Calibration of a Nose Boom Mounted Airflow Sensor on an Atmospheric Research Aircraft by Inflight Maneuvers, DLR-FB-2021-17, https://elib.dlr.de/145969.

Gill, A.E. (1982), Atmosphere and Ocean Dynamics, Academic Press, New York.

Grinsted, A., Moore, J. C., and Jevrejeva, S. (2004), Application of the cross wavelet transform and wavelet coherence to geophysical time series, *Nonlin. Processes Geophys.*, *11*, 561–566, doi:10.5194/npg-11-561-2004.

Hendricks, E. A., J. D. Doyle, S. D. Eckermann, Q. Jiang, and P. A. Reinecke (2014), What is the source of the stratospheric gravity wave belt in austral winter?, *J. Atmos. Sci.*, *71*, 1583–1592, doi:10.1175/JAS-D-13-0332.1.

Hertzog, A., Boccara, G., Vincent, R. A., Vial, F., and Cocquerez, P. (2008), Estimation of Gravity Wave Momentum Flux and Phase Speeds from Quasi-Lagrangian Stratospheric Balloon Flights. Part II: Results from the Vorcore Campaign in Antarctica, *J. Atmos. Sci.*, *65*, 3056–3070, doi:10.1175/2008JAS2710.1.

Hindley, N.P., Wright, C.J., Smith, N.D., and Mitchell, N.J. (2015), The southern stratospheric gravity wave hotspot: individual waves and their momentum fluxes measured by COSMIC GPS-RO, *Atmos. Chem. Phys.*, *15*, 7797–7818, doi:10.5194/acp-15-7797-2015.

Hoffmann, L., Grimsdell, A. W., and Alexander, M. J. (2016), Stratospheric gravity waves at Southern Hemisphere orographic hotspots: 2003 –2014 AIRS/Aqua observations, *Atmos. Chem. Phys.*, *16*, 9381–9397, doi:10.5194/acp-16-9381-2016.

John, S. R. and Kumar, K. K. (2013), A discussion on the meth- ods of extracting gravity wave perturbations from space- based measurements, *Geophys. Res. Lett.*, *40*, 2406–2410, doi:10.1002/grl.50451.

816 Kaifler, B., Büdenbender, C., Mahnke, P., Damm, M., Sauder, D., Kaifler, N., and Rapp, M.
817 (2017), Demonstration of an iron fluorescence lidar operating at 372 nm wavelength using
818 a newly-developed Nd:YAG laser, *Opt. Lett.*, *42*, 2858–2861, doi:10.1364/OL.42.002858.
819 Kaifler, N., Kaifler, B., Dörnbrack, A. et al. (2020), Lidar observations of large-amplitude
820 mountain waves in the stratosphere above Tierra del Fuego, Argentina, *Sci. Rep.*, *10*,
821 14529, doi:10.1038/s41598-020-71443-7.
822 Kaifler, B. and Kaifler, N. (2021), A Compact Rayleigh Autonomous Lidar (CORAL) for the
823 middle atmosphere, *Atmos. Meas. Tech.*, *14*, 1715–1732, doi:10.5194/amt-14-1715-2021.
824 Kaifler et al.(2022). To be submitted to the same special issue. A case study of mountain
825 wave momentum flux measurements in the middle atmosphere over the southern Andes.
826 Kruse, C. G., and Smith, R. B. (2015), Gravity Wave Diagnostics and Characteristics in
827 Mesoscale Fields, *J. Atmos. Sci.*, *72*, 4372–4392, doi:10.1175/JAS-D-15-0079.1.
828 Kruse, C. G., R. B. Smith, and S. D. Eckermann (2016), The Midlatitude Lower-
829 Stratospheric Mountain Wave Ṽalve Layer, *J. Atmos. Sci.*, *73*, 5081–5100,
830 doi:10.1175/JAS-D-16-0173.1.
831 Llamedo, P., Salvador, J., de la Torre, A., Quiroga, J., Alexander, P., Hierro, R., et al. (2019),
832 11 years of Rayleigh lidar observations of gravity wave activity above the southern tip of
833 South America, *J. Geophys. Res. Atmos.*, *124*, 451–467, doi:10.1029/2018JD028673.
834 Lu, X., C. Chen, W. Huang, J. A. Smith, X. Chu, T. Yuan, P.-D. Pautet, M. J. Taylor, J. Gong,
835 and C. Y. Cullens (2015), A coordinated study of 1 h mesoscale gravity waves propagating
836 from Logan to Boulder with CRRL Na Doppler lidars and temperature mapper, *J. Geo-*
837 *phys. Res. Atmos.*, *120*, 10,006–10,021, doi:10.1002/2015JD023604.
838 McLandress, C., Shepherd, T.G., Polavarapu, S. and Beagley, S.R. (2012), Is Missing Oro-
839 graphic Gravity Wave Drag near 60^oS the Cause of the Stratospheric Zonal Wind Bi-
840 ases in Chemistry–Climate Models?, *J. Atmos. Sci.*, *69*, 802–818, doi:10.1175/JAS-D-
841 11-0159.1.
842 Nappo, C. J. (2012), An introduction to atmospheric gravity waves, 2nd edition, Academic
843 Press, London.
844 Nash, E. R., Newman, P. A., Rosenfield, J. E., and Schoeberl, M. R. (1996), An objective
845 determination of the polar vortex using Ertels potential vorticity, *J. Geophys. Res.*, *101*,
846 9471–9478, doi:10.1029/96JD00066.
847 Plougonven, R., H. Teitelbaum, and V. Zeitlin (2003), Inertia-gravity wave generation by the
848 tropospheric midlatitude jet as given by the Fronts and Atlantic Storm-Track Experiment

radio soundings, *J. Geophys. Res.*, *108*, 4686, doi:10.1029/2003JD003535.

Plougonven, R., Hertzog, A., and Teitelbaum, H. (2008), Observations and simulations of a large-amplitude mountain wave breaking over the Antarctic Peninsula, *J. Geophys. Res.*, *113*, D16113, doi:10.1029/2007JD009739.

Plougonven R, Hertzog A, Guez L. (2013), Gravity waves over Antarctica and the Southern Ocean: consistent momentum fluxes in mesoscale simulations and stratospheric balloon observations, *Q. J. R. Meteorol. Soc.*, *139*, 101–118, doi:10.1002/qj.1965.

Plougonven, R., and F. Zhang (2014), Internal gravity waves from atmospheric jets and fronts, *Rev. Geophys.*, *52*, 33–76, doi:10.1002/2012RG000419.

Plougonven, R., Hertzog, A., and Alexander, M. J. (2015), Case studies of nonorographic gravity waves over the southern ocean emphasize the role of moisture, *J. Geophys. Res. Atmos.*, *120*, 1278–1299, doi:10.1002/2014JD022332.

Preusse, P., Schroeder, S., Hoffmann, L., Ern, M., Friedl-Vallon, F., Ungermann, J., Oelhaf, H., Fischer, H., and Riese, M. (2009), New perspectives on gravity wave remote sensing by spaceborne infrared limb imaging, *Atmos. Meas. Tech.*, *2*, 299–311, doi:10.5194/amt-2-299-2009.

Preusse, P., Ern, M., Bechtold, P., Eckermann, S. D., Kalisch, S., Trinh, Q. T., and Riese, M. (2014), Characteristics of gravity waves resolved by ECMWF, *Atmos. Chem. Phys.*, *14*, 10483–10508, doi:10.5194/acp-14-10483-2014.

Queney, P. (1948), The Problem of Air Flow Over Mountains: A Summary of Theoretical Studies, *B. Am. Meteorol. Soc.*, *29*, 16–26, doi:10.1175/1520-0477-29.1.16.

Rapp, M., Kaifler, B., Dörnbrack, A., Gisinger, S., Mixa, T., Reichert, R., Kaifler, N., Knobloch, S., Ecbert, R., Wildmann, N., Giez, A., Krasauskas, L., Preusse, P., Geldenhuys, M., Riese, M., Woiwode, W., Friedl-Vallon, F., Sinnhuber, B., de la Torre, A., Alexander, P., Hormaechea, J. L., Janches, D., Garhammer, M., Chau, J. L., Conte, F., Hoor, P., and Engel, A. (2021), SOUTHTRAC-GW: An airborne field campaign to explore gravity wave dynamics at the world's strongest hotspot, *B. Am. Meteorol. Soc.*, *102*, E871–E893, doi:10.1175/BAMS-D-20-0034.1.

Reichert, R., Kaifler, B., Kaifler, N., Dörnbrack, A., Rapp, M., and Hormaechea, J. L. (2021), High-cadence lidar observations of middle atmospheric temperature and gravity waves at the Southern Andes hot spot, *J. Geophys. Res.*, *126*, e2021JD034683, doi:10.1029/2021JD034683.

Satomura, T. and Sato, K. (1999), Secondary Generation of Gravity Waves Associated with the Breaking of Mountain Waves, *J. Atmos. Sci.*, *56*, 3847–3858, doi:10.1175/1520-0469(1999)056<3847:SGOGWA>2.0.CO;2.

Sato, K., Tateno, S., Watanabe, S., and Kawatani, Y. (2012), Gravity Wave Characteristics in the Southern Hemisphere Revealed by a High-Resolution Middle-Atmosphere General Circulation Model, *J. Atmos. Sci.*, *69*, 1378–1396, doi:10.1175/JAS-D-11-0101.1.

Scorer, R. S. (1949), Theory of waves in the lee of mountains, *Q. J. Roy. Meteor. Soc.*, *75*, 41–56, doi:10.1002/qj.49707532308.

Skamarock, W., , and J. B. Klemp (2008), A time-split nonhydrostatic atmospheric model for weather research and forecasting applications, *J. Comput. Phys.*, *227*, 3465–3485, doi:10.1016/j.jcp.2007.01.037.

Smith, R. B., Woods, B. K., Jensen, J., Cooper, W. A., Doyle, J. D., Jiang, Q., and Grubišić, V. (2008), Mountain waves entering the stratosphere, *J. Atmos. Sci.*, *65*, 2543–2562, doi:10.1175/2007JAS2598.1.

Smith, R. B., Nugent, A. D., Kruse, C. G., Fritts, D. C., Doyle, J. D., Eckermann, S. D., Taylor, M. J., Dörnbrack, A., Uddstrom, M., Cooper, W., Romashkin, P., Jensen, J., and Beaton, S. (2016). Stratospheric Gravity Wave Fluxes and Scales during DEEPWAVE, *J. Atmos. Sci.*, *73*, 7, 2851–2869, doi:10.1175/JAS-D-15-0324.1.

Torrence, C., and Compo, G.P. (1998), A practical guide to wavelet analysis, *Bull. Am. Meteorol. Soc.*, *79*, 61–78, doi:10.1175/1520-0477(1998)079<0061:APGTWA>2.0.CO;2.

Uccellini, L. W., and S. E. Koch (1987), The synoptic settings and possible energy sources for mesoscale wave disturbances, *Mon. Weather. Rev.*, *115*, 721–729, 10.1175/1520-0493(1987)115<0721:TSSAPE>2.0.CO;2.

Vadas, S. L. (2013), Compressible f-plane solutions to body forces, heatings, and coolings, and application to the primary and secondary gravity waves generated by a deep convective plume, *J. Geophys. Res. Space Physics*, *118*, 2377–2397, doi:10.1002/jgra.50163.

Wagner, J., Dörnbrack, A., Rapp, M., Gisinger, S., Ehard, B., Bramberger, M., Witschas, B., Chouza, F., Rahm, S., Mallaun, C., Baumgarten, G., and Hoor, P. (2017), Observed versus simulated mountain waves over Scandinavia – improvement of vertical winds, energy and momentum fluxes by enhanced model resolution?, *Atmos. Chem. Phys.*, *17*, 4031–4052, doi:10.5194/acp-17-4031-2017.

Wildmann, N., R. Eckert, A. Dṙnbrack, S. Gisinger, A. van Niekerk, K. Ohlmann, and M. Rapp (2021), In situ measurements of wind and turbulence by a motor glider in the Andes,

914 *J. Atmos. Oceanic Technol.*, *38*,921–935, doi:10.1175/JTECH-D-20-0137.1.

915 Wright, C., Hindley, N., Moss, A. and Mitchell, N. (2016), Multi-instrument gravity-wave
916 measurements over Tierra del Fuego and the Drake Passage — Part 1: potential energies
917 and vertical wavelengths from AIRS, COSMIC,HIRDLS, MLS-Aura, SAAMER, SABER
918 and radiosondes, *Atmos. Meas. Tech.*, *9*, 877–908, doi:10.5194/amt-9-877-2016.

919 Zhao, J., Chu, X., Chen, C., Lu, X., Fong, W., Yu, Z., et al. (2017), Lidar observations of
920 stratospheric gravity waves from 2011 to 2015 at McMurdo (77.84^{o}S, 166.69^{o}E), Antarc-
921 tica: 1. Vertical wavelengths, periods, and frequency and vertical wavenumber spectra, *J.*
922 *Geophys. Res. Atmos.*, *122*, 5041–5062, doi:10.1002/2016JD026368.

923 **Table 1.** Vertical gravity wave energy flux EF for legs 1, 2, 4 and 6 calculated directly and through the
924 momentum flux with BAHAMAS and WRF data.

	BAHAMAS		WRF	
Leg	$-(\overline{u}MF_x + \overline{v}MF_y)$/(W m^{-2})	EF/(W m^{-2})	$-(\overline{u}MF_x + \overline{v}MF_y)$/(W m^{-2})	EF/(W m^{-2})
1	2.0	1.8	0.5	0.8
2	-1.2	1.5	0.7	0.4
4	0.4	1.6	0.5	1.1
6	1.2	1.3	0.4	0.2

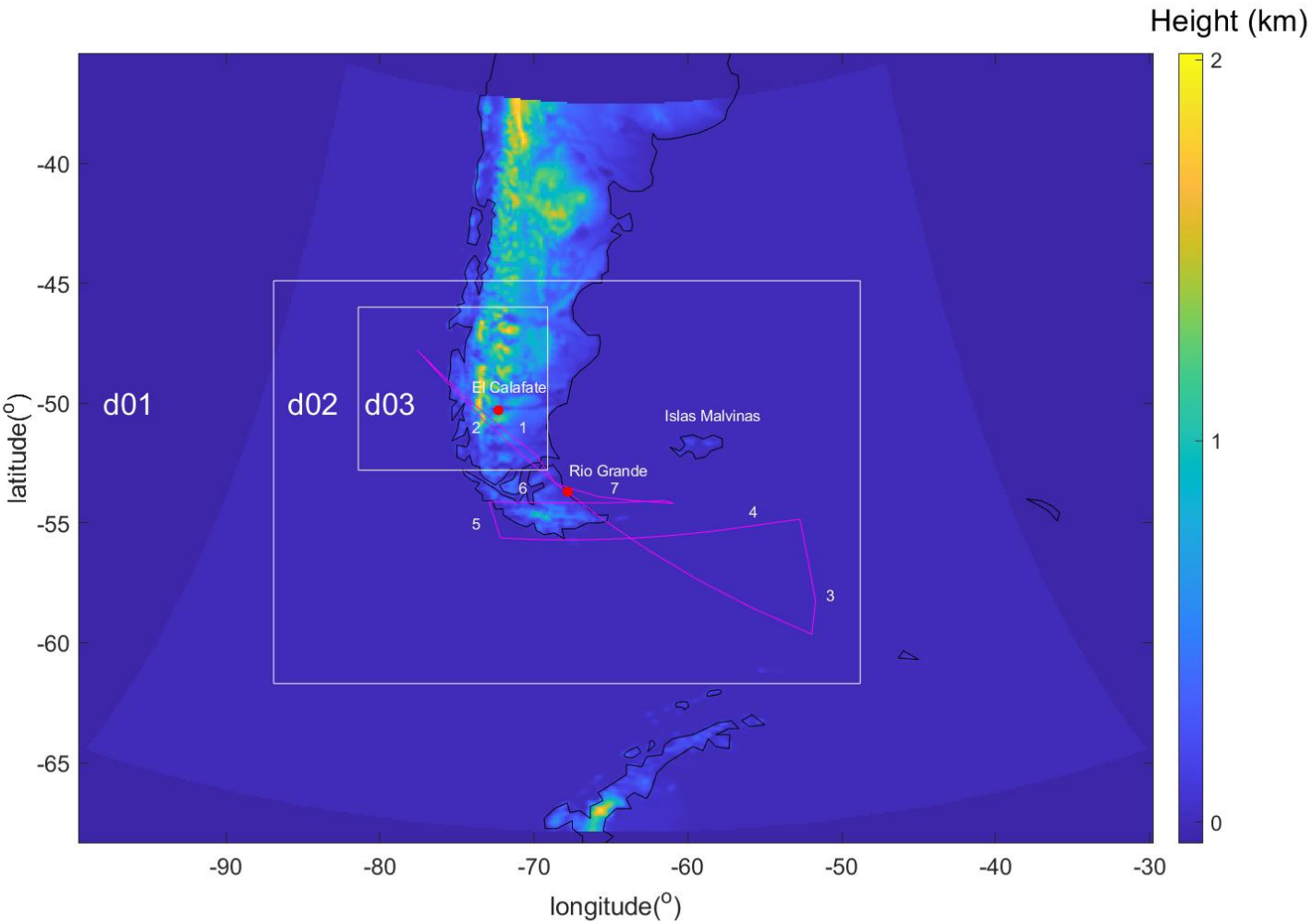

925 **Figure 1.** The ST08 flight trajectory and the number associated to each leg are shown. The three nested
926 domains d01, d02 and d03 used with the WRF numerical model are included. For clarity the Lambert projec-
927 tion used in the simulations is only drawn for the largest zone. Its general shape is the same in the other two
928 domains.

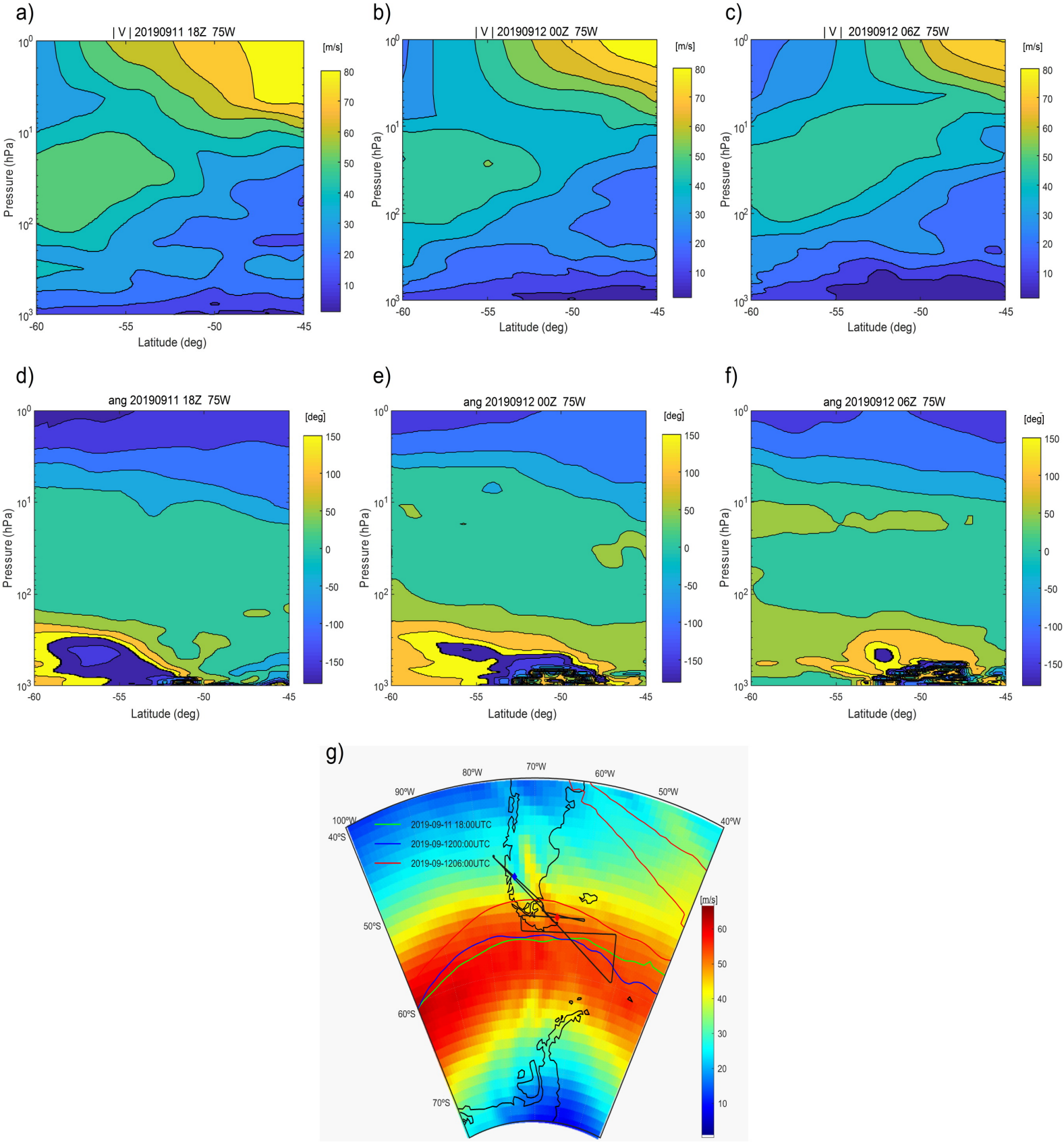

Figure 2. On September 11 18 UTC and September 12 00 and 06 UTC: a-c) absolute value of horizontal wind at 75W, d-f) angle of horizontal wind at 75W (measured as from East direction), g) Magnitude of horizontal wind only on September 12 00 UTC and vortex location, both quantities at 475 K isentropic level.

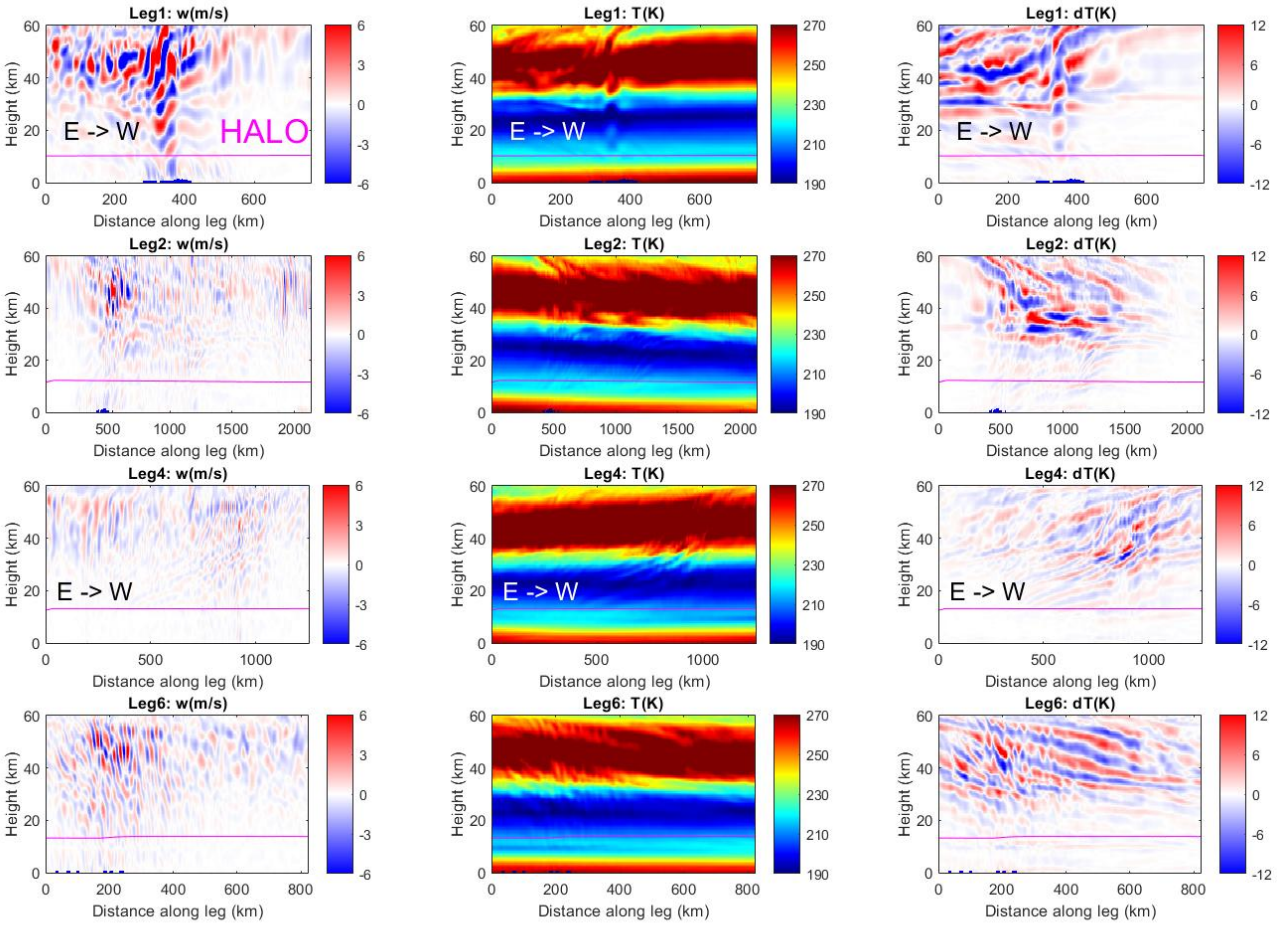

932 **Figure 3.** WRF vertical cross sections of w, T and dT (for horizontal wavelengths shorter than 500 km)
933 along the four studied flight legs as indicated per panel. The aircraft trajectory is also shown. The lower blue
934 part is a rough representation of topography.

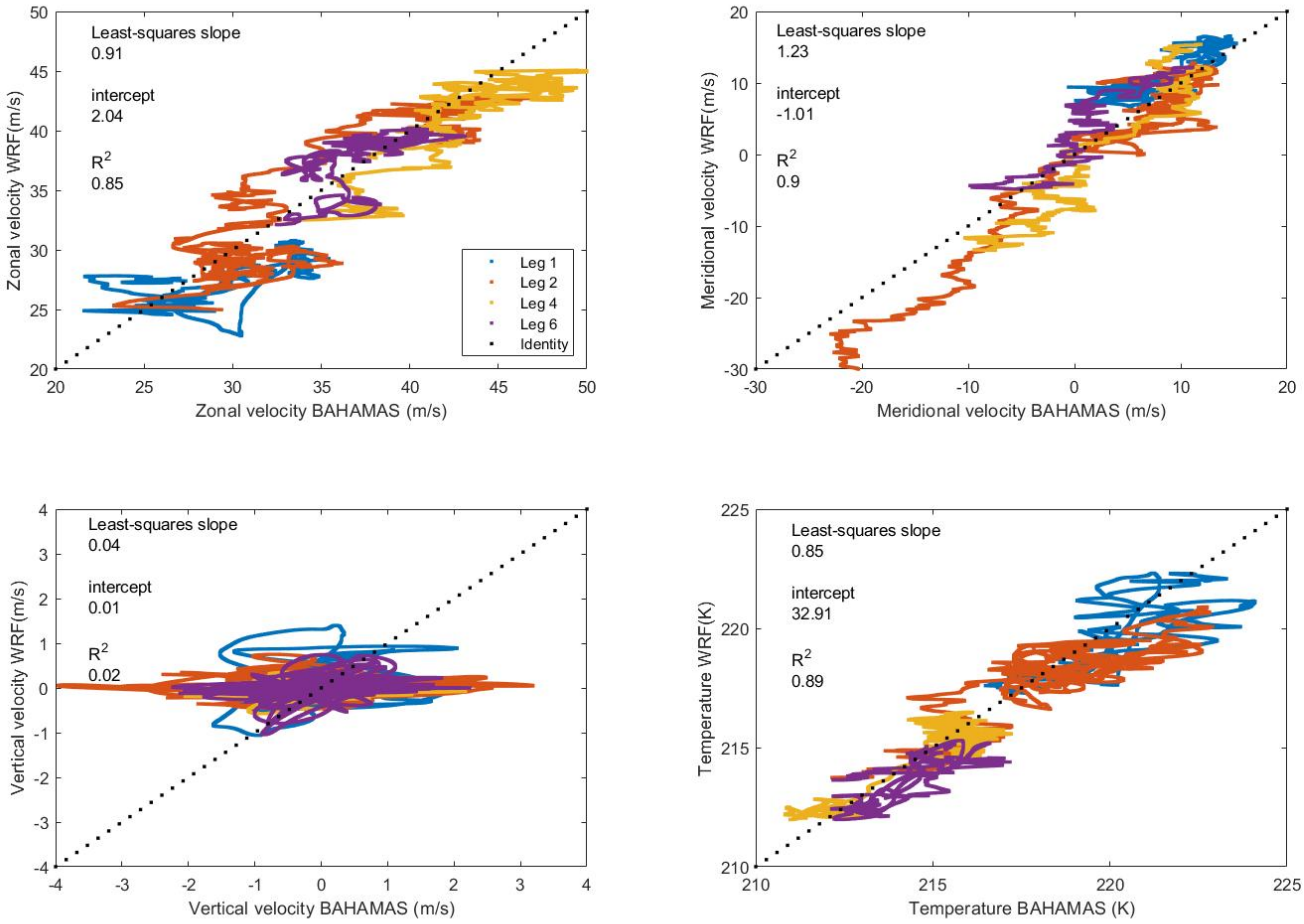

Figure 4. Relationship between BAHAMAS and WRF u, v, w and T at the same time and position for the four studied legs. Regression results and the ideal identity line are also shown.

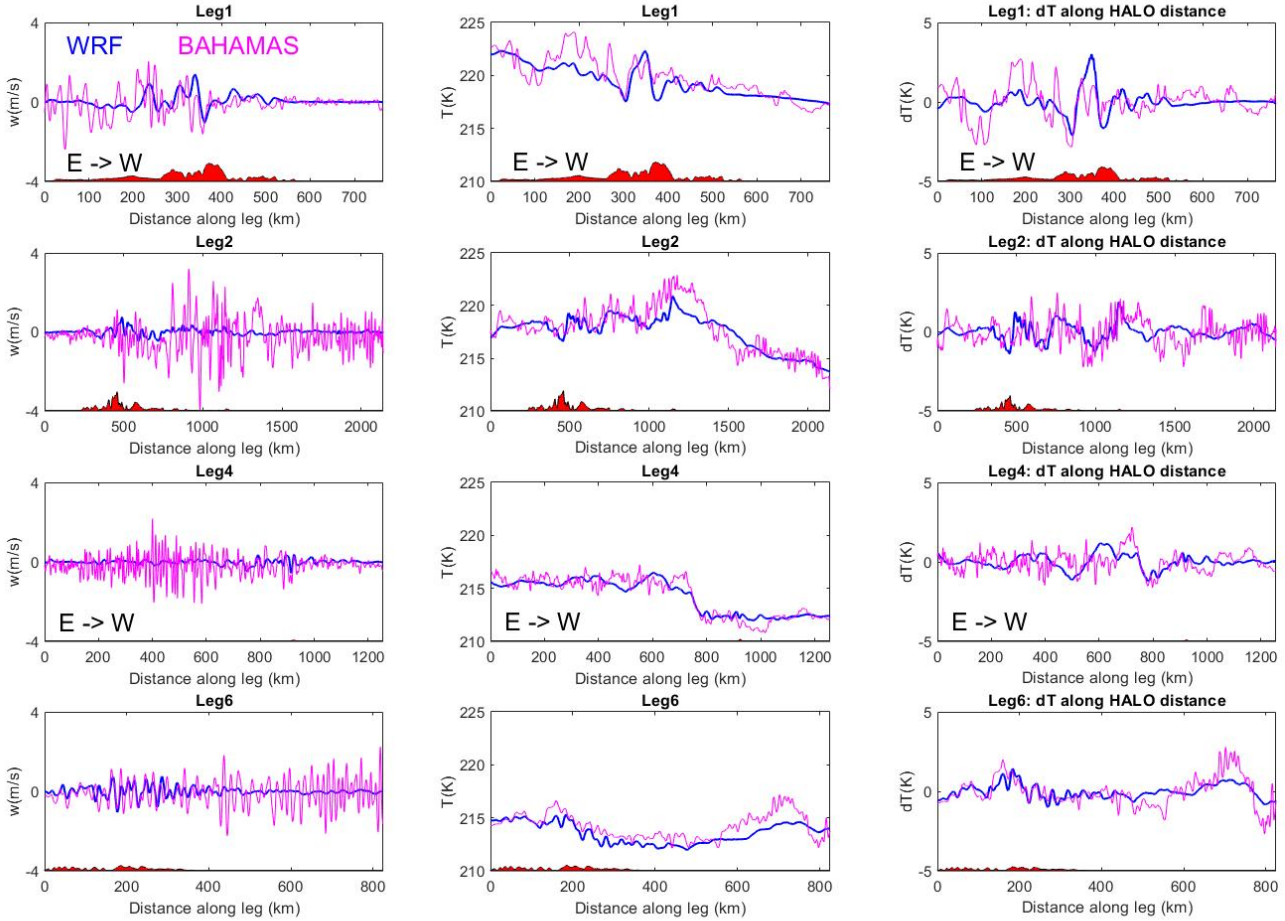

Figure 5. WRF and BAHAMAS w, T and dT (along the aircraft path) at flight level in the four analyzed segments as indicated in each panel. The lower red part represents topography in an arbitrary scale.

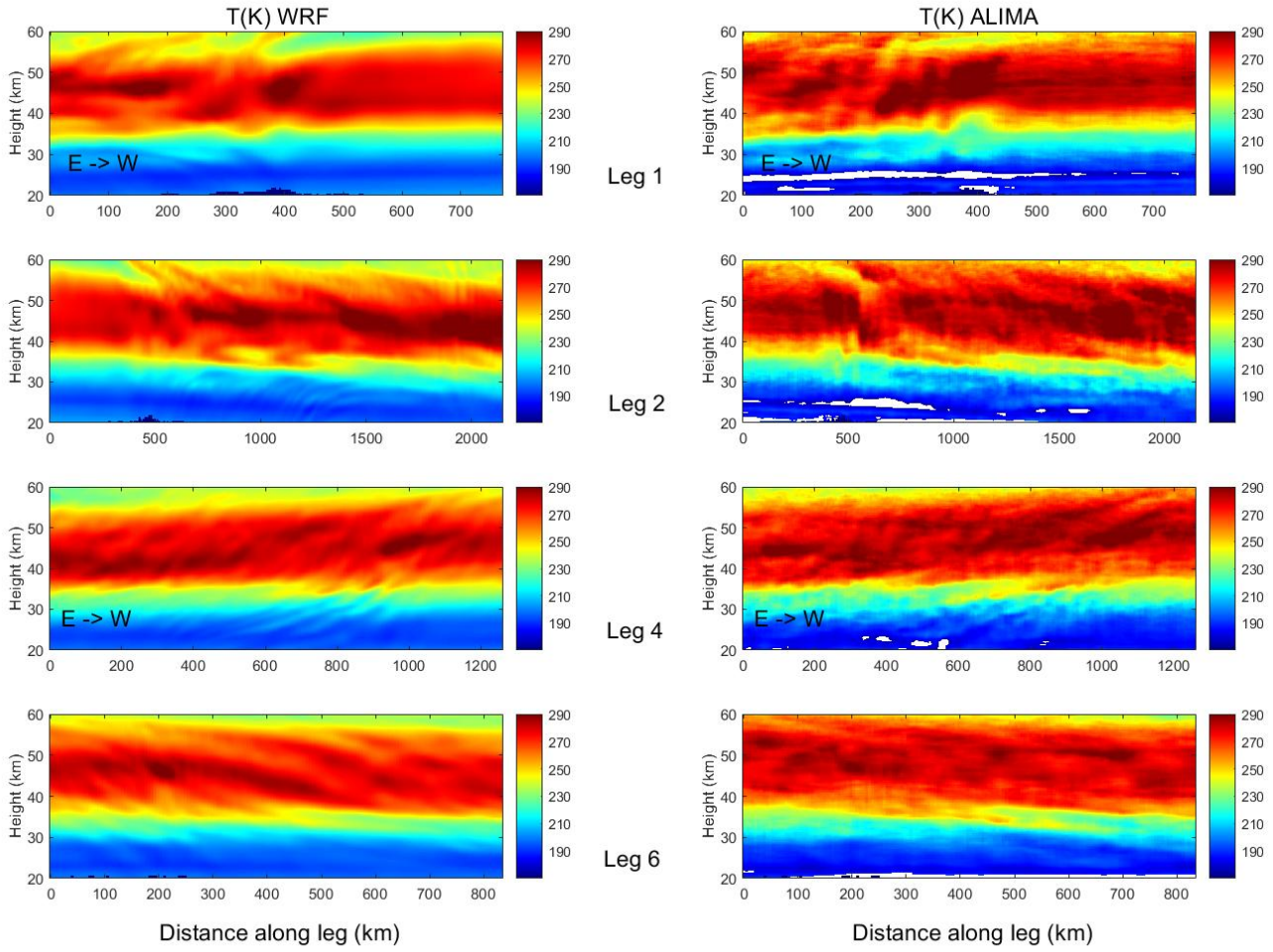

939 **Figure 6.** Comparison of vertical cross sections of T in the common vertical range of ALIMA and WRF
940 along the four analyzed legs. The lower blue part is a rough representation of topography. White parts in blue
941 sectors correspond to zones where ALIMA cannot measure temperature due to polar stratospheric clouds.

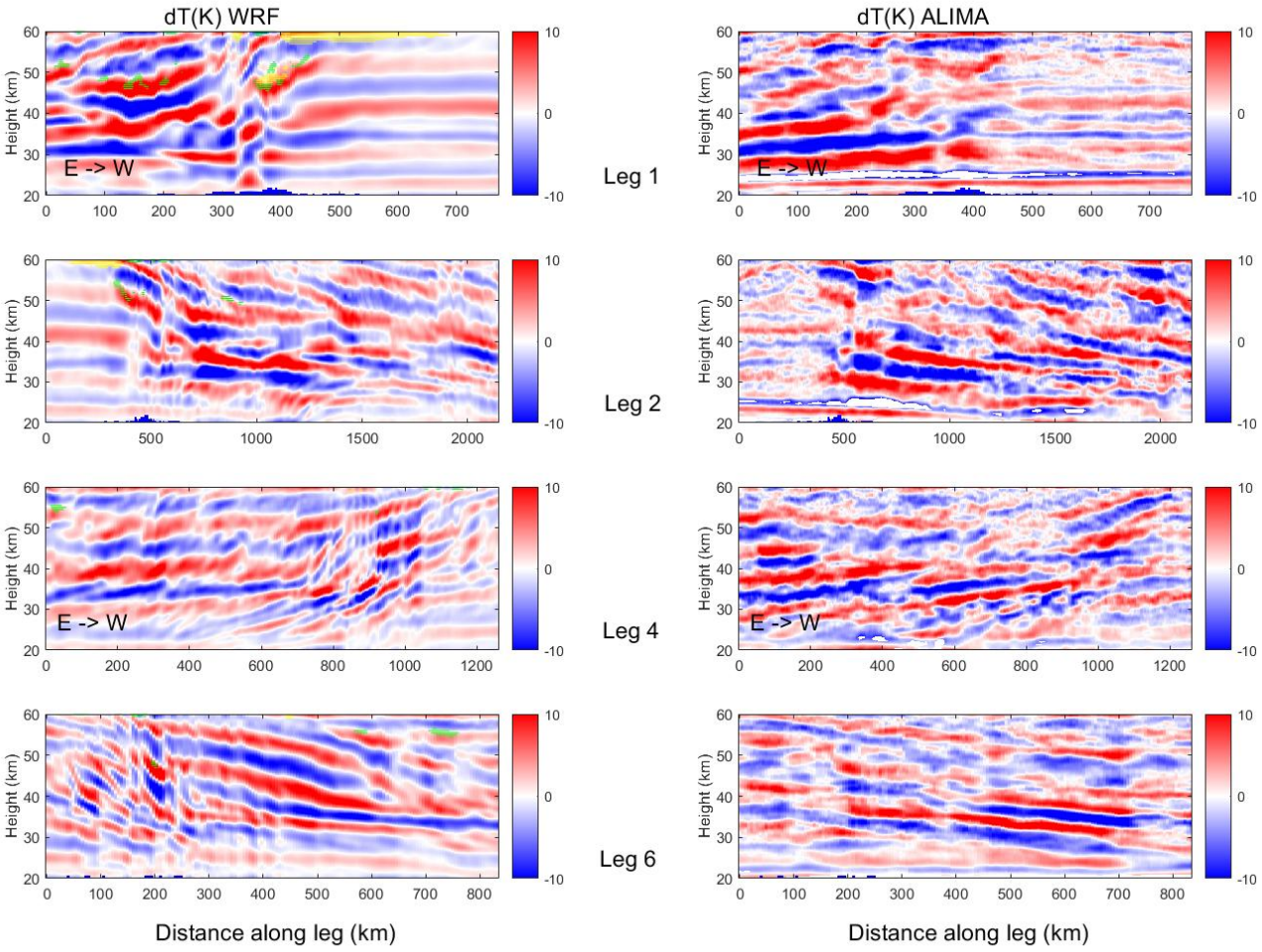

Figure 7. The same as Figure 6 for dT vertically filtered between 2 and 20 km. White parts in blue parcels correspond to zones where ALIMA cannot measure temperature due to polar stratospheric clouds. Green sectors correspond to Ri < 0.25 and yellow zones to $L^2 < 0$ as calculated from WRF.

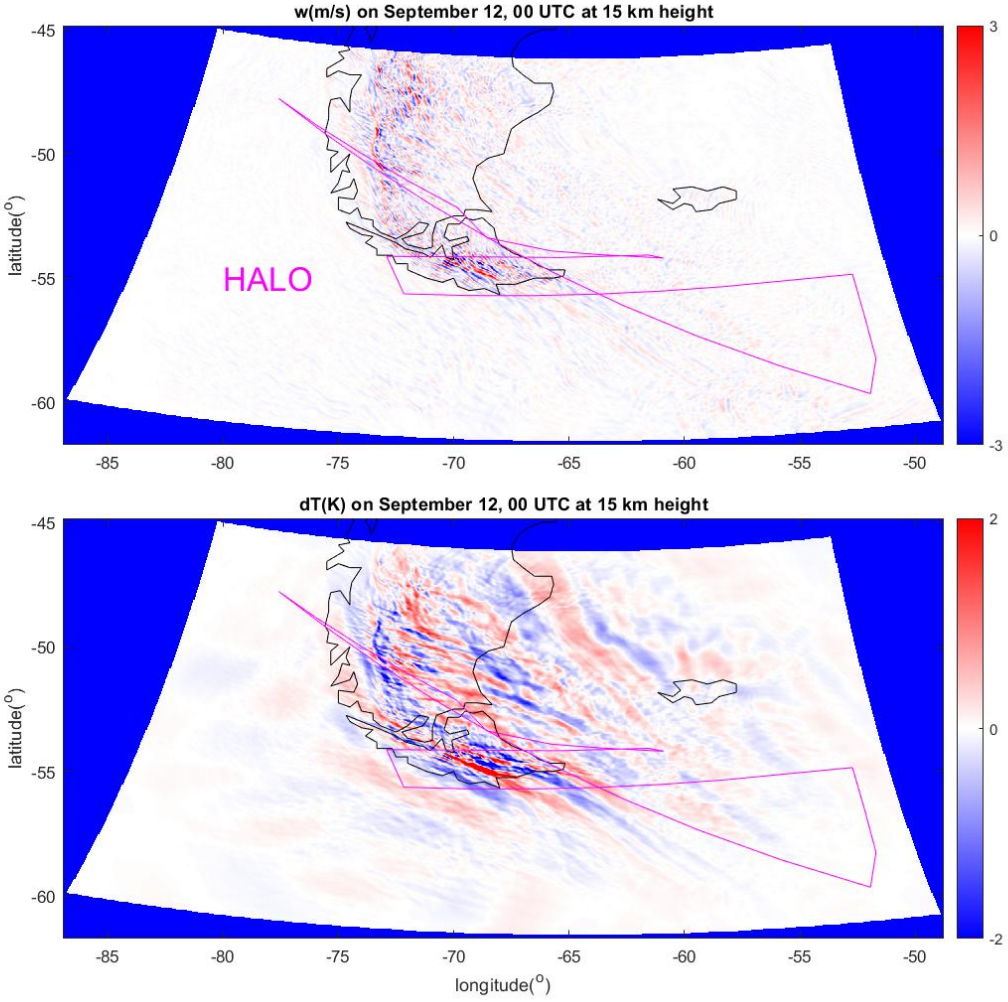

945 **Figure 8.** WRF horizontal cross section at 15 km height for w and dT with an horizontal filter cutoff of 500

946 km on September 12 at 00 UTC.

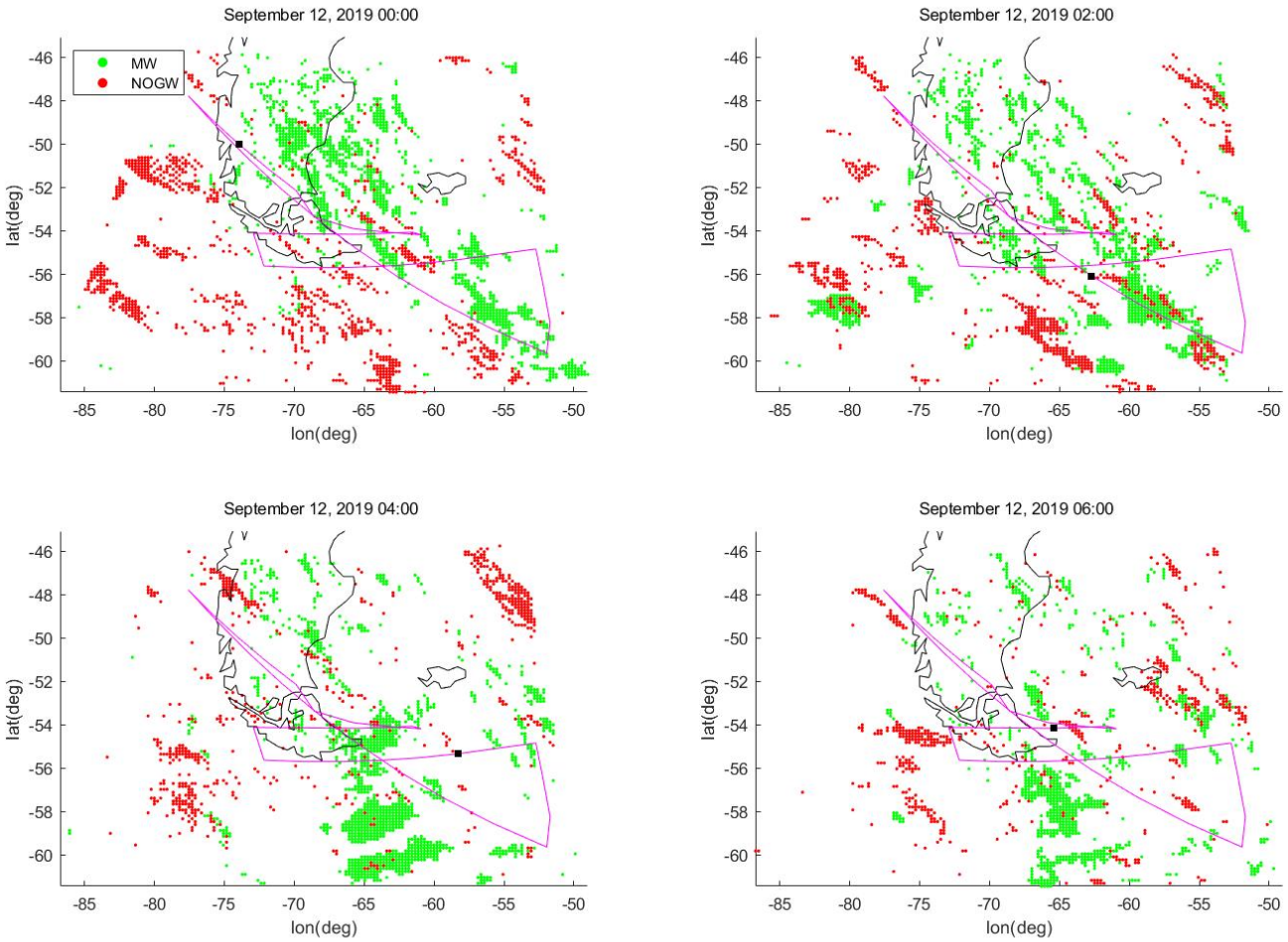

Figure 9. Points in the WRF simulations on September 12 at 00, 02, 04 and 06 UTC where the verification of the polarization relation for both horizontal velocity perturbation components along a vertical column from the ground to 60 km height (coherence above 0.9) determines that it resembles a MW or NOGW. The HALO trajectory (magenta line) and the instantaneous position (black square) are also shown.

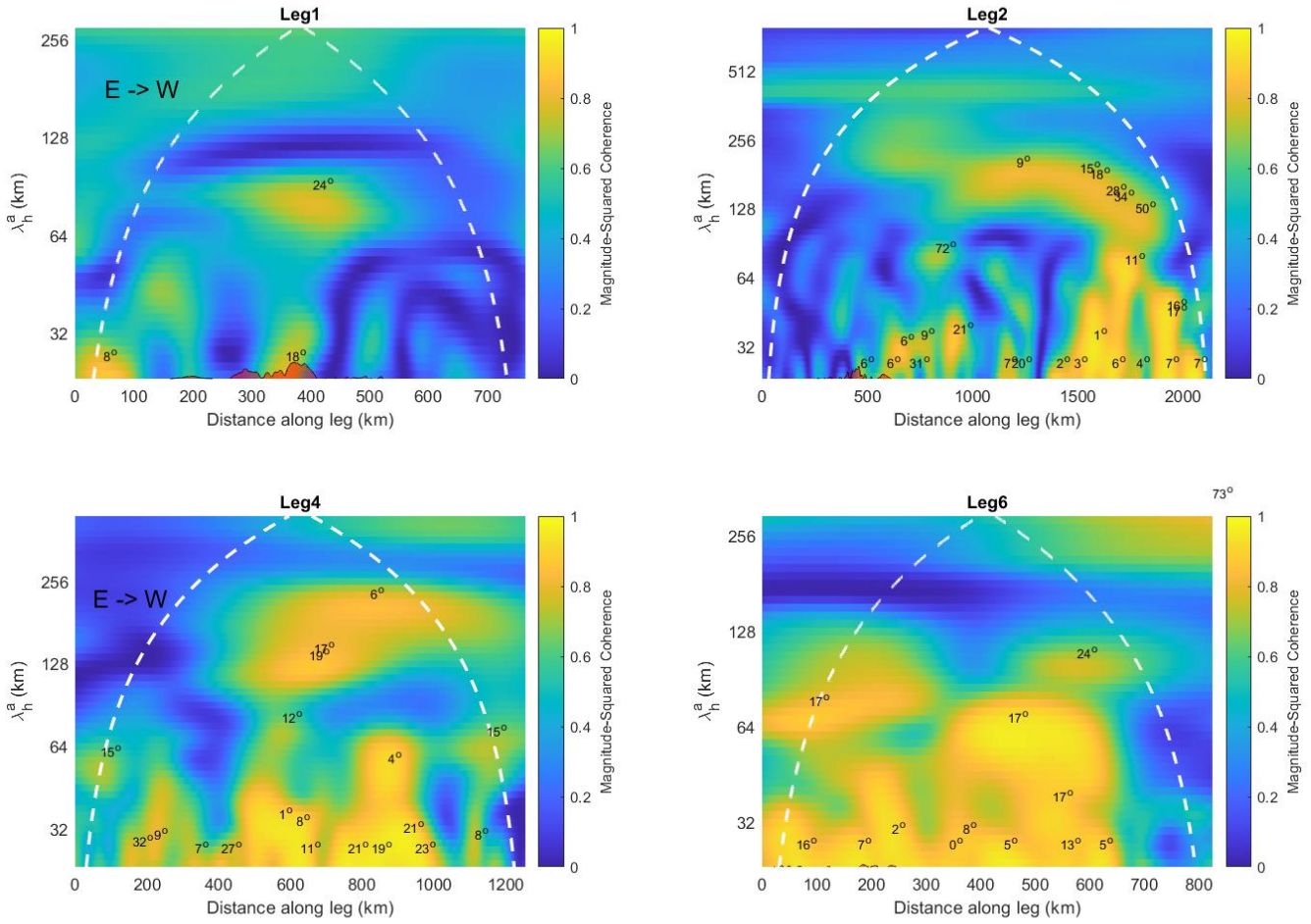

951 **Figure 10.** BAHAMAS *w* and *T* wavelet magnitude-squared coherence for apparent horizontal wavelengths
952 longer than 24 km as seen from the aircraft trajectory. Where the coherence stays above 0.7 it includes the
953 phase difference departure from 90^o (ideal GW) at the location of maximal correspondence between both
954 quantities. White dashed lines indicate the limits of the so-called cone of influence where artifacts may start
955 affecting the results. Topography is shown in red and not to scale.

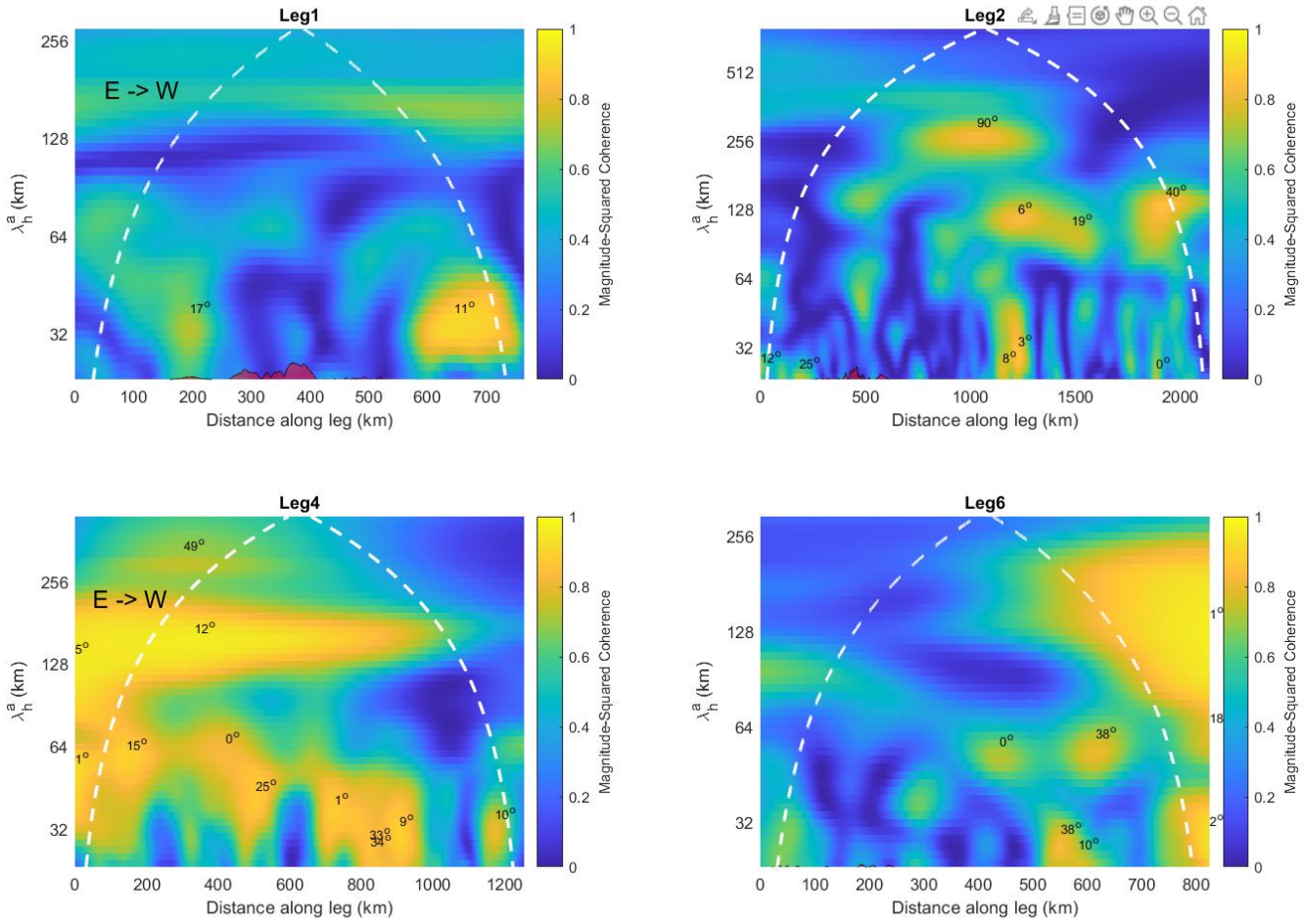

Figure 11. Similar to Figure 10 but for BAHAMAS *u* and *v* and it shows phase difference departure from 0^o or 180^o (ideal linear MW).

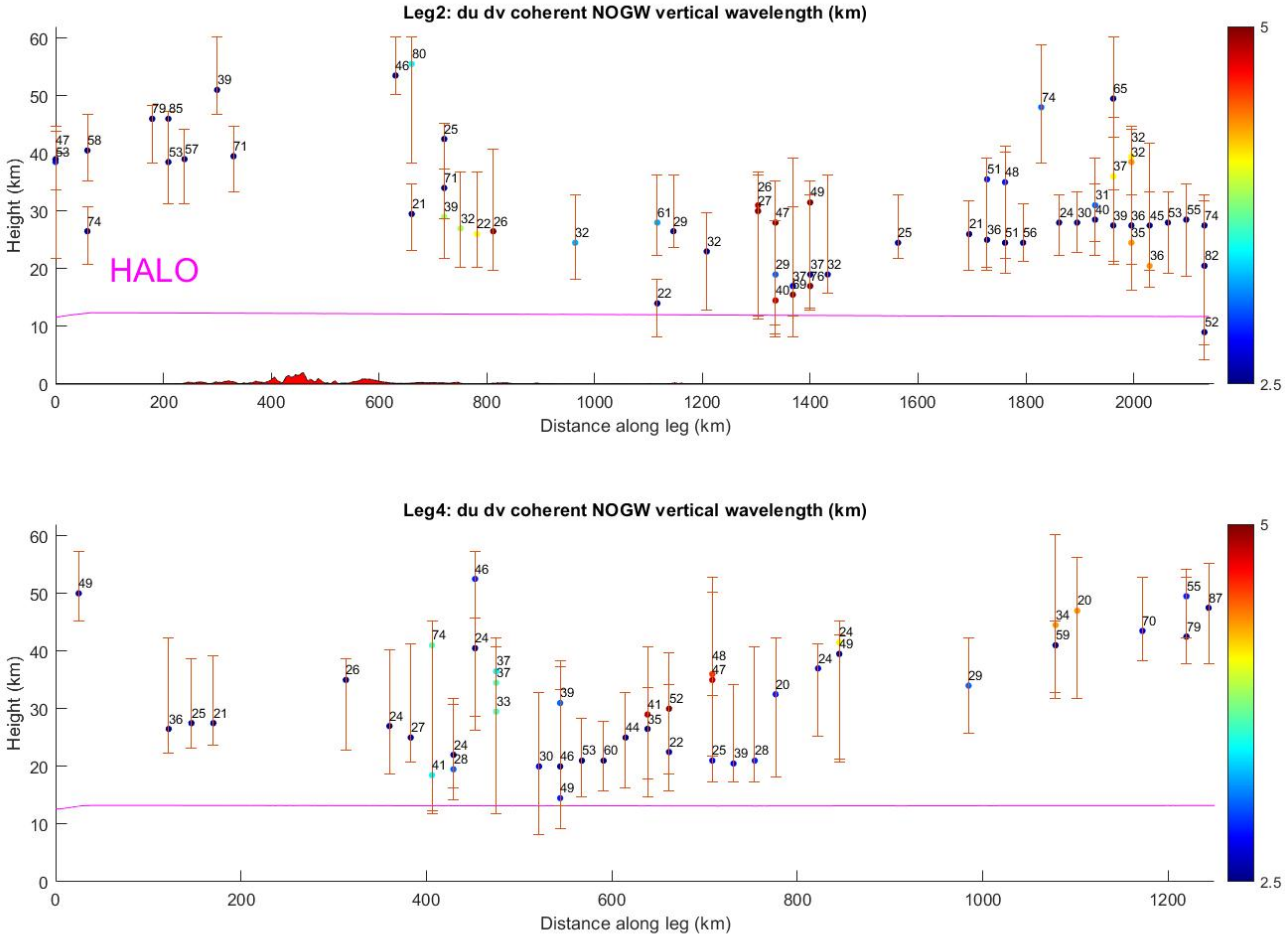

Figure 12. Flight points along segments 2 and 4 where the coherence of both WRF horizontal velocity perturbation components in the vertical columns 0 to 60 km stays above 0.7. It is evaluated every 30 km of aircraft trajectory. The colors identify the optimal vertical wavelength. Numbers indicate the phase difference at the height of maximal relationship and the vertical intervals show where the coherence stays above 0.7. A minimum of 4 turns is required for the identification of NOGW. Topography is also shown in the lower part of the panels.

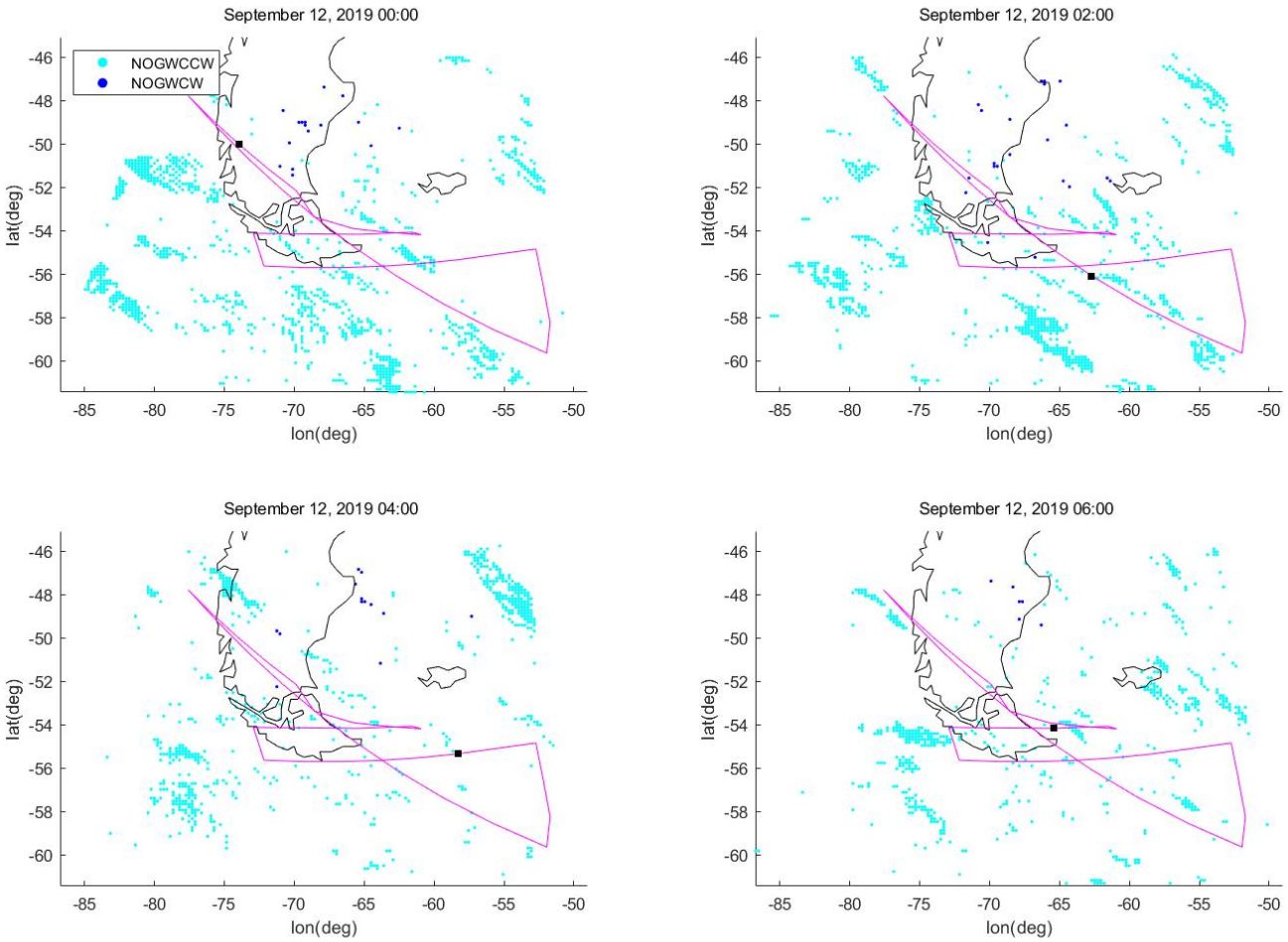

964 **Figure 13.** Points in the WRF simulations on September 12 at 00, 02, 04 and 06 UTC where the verifica-
965 tion of the polarization relation for both horizontal velocity perturbation components along a vertical column
966 (coherence above 0.9) determines that it resembles a clockwise (CW) or counterclockwise (CCW) NOGW.
967 The HALO trajectory (magenta line) and the instantaneous position (black square) are also shown.

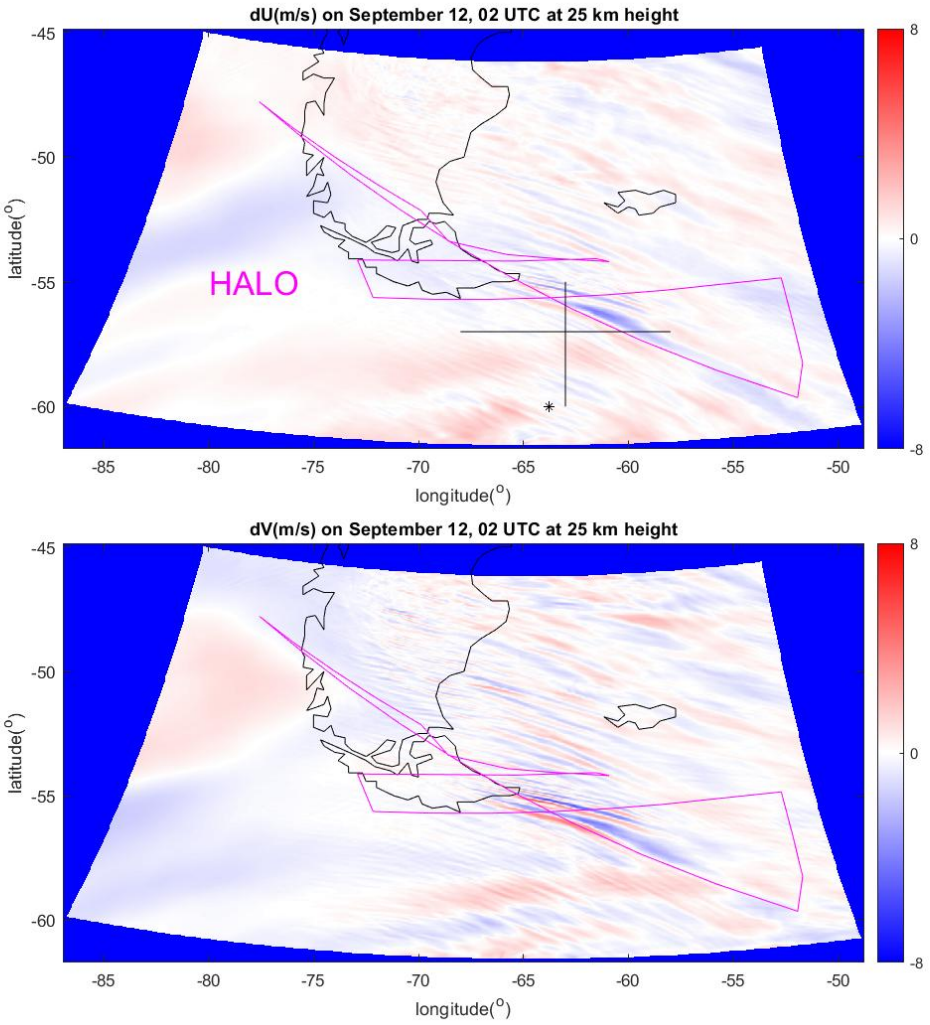

968 **Figure 14.** Horizontal cross sections for both WRF horizontal velocity perturbations vertically filtered
969 between 2 and 5 km at 25 km height on September 12, 02 UTC.

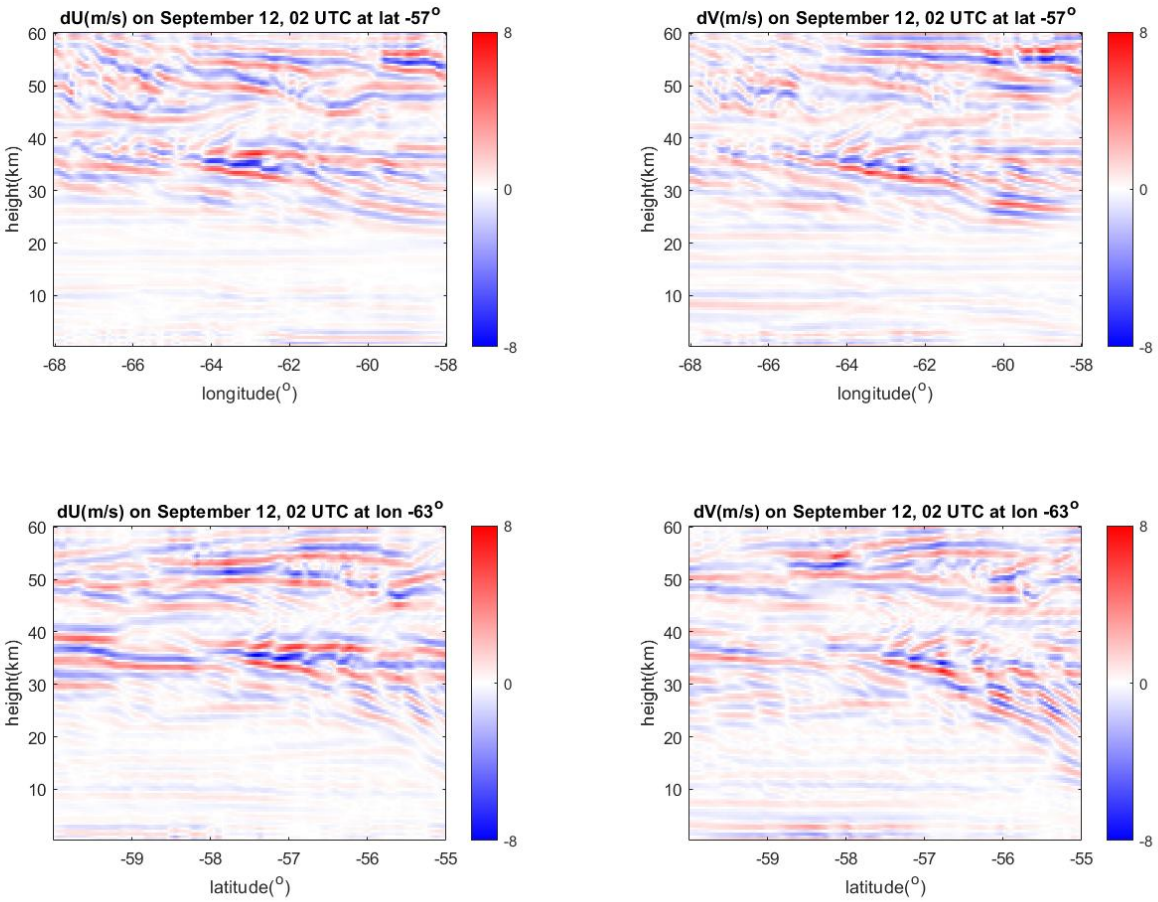

970 **Figure 15.** Vertical cross sections as located in the black cross in the upper panel of Figure 14 for both
971 WRF horizontal velocity perturbations vertically filtered between 2.5 and 5 km on September 12, 02 UTC.

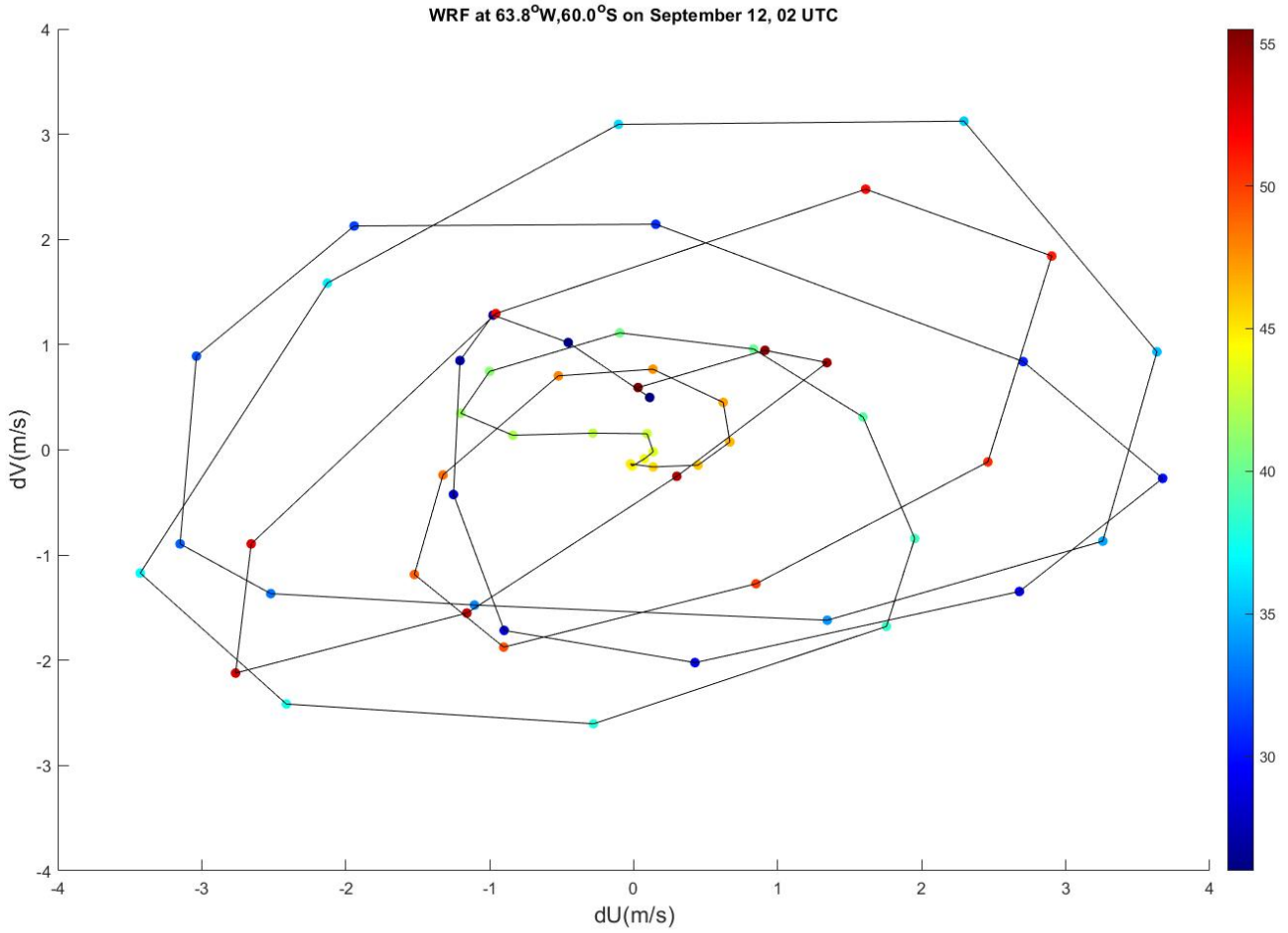

Figure 16. Elliptical rotation with height of the WRF horizontal velocity perturbation vector in the black asterisk shown in the upper panel of Figure 14 on September 12, 02 UTC.

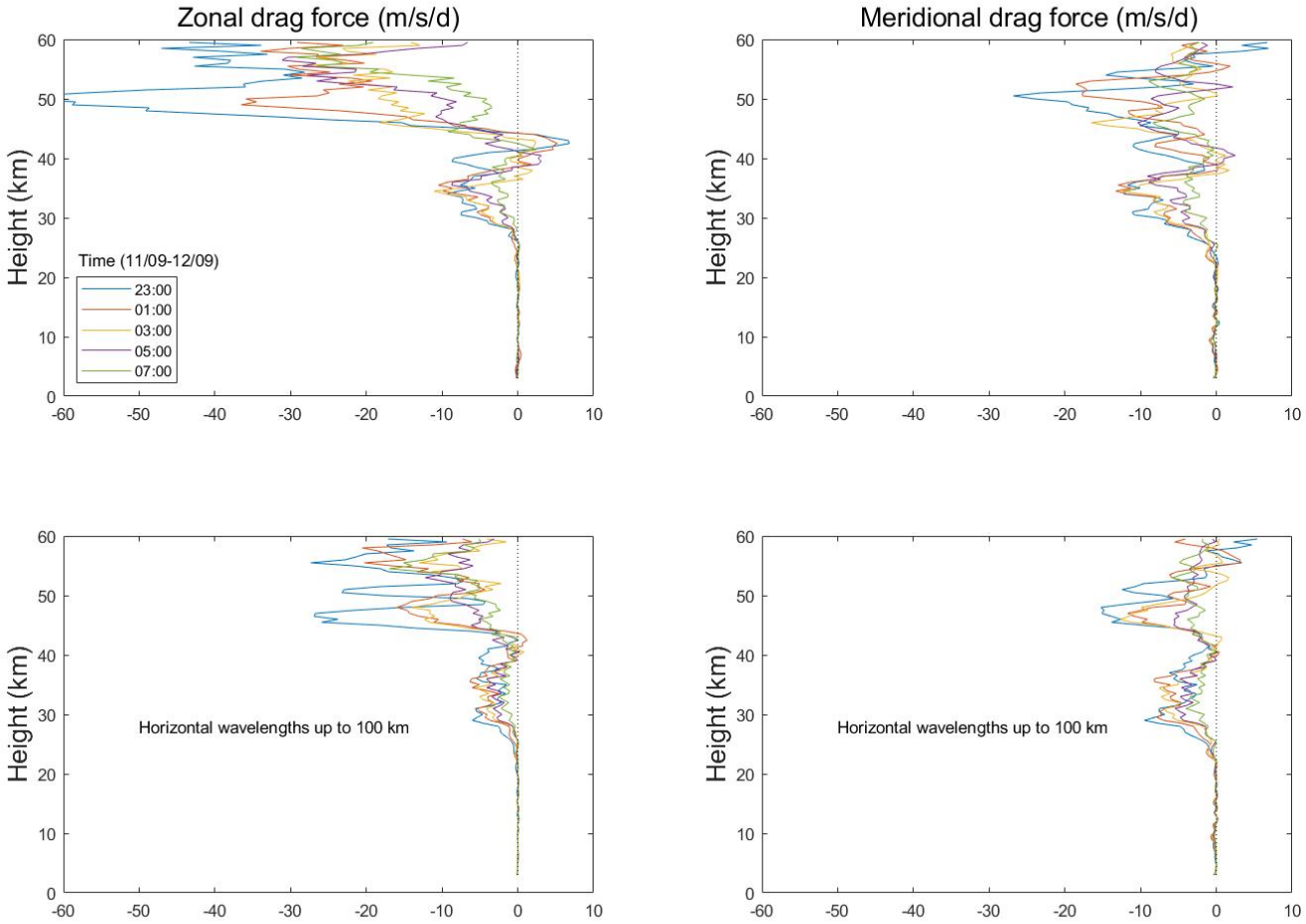

974 **Figure 17.** The zonal and meridional drag components as obtained from WRF simulations every 2 hours
975 from September 11, 23 UTC to September 12, 07 UTC in the rectangle defined by 77W, 63W, 60S and 45S.
976 The two top and two lower panels correspond respectively to the contribution of horizontal wavelengths
977 shorter than 500 km and 100 km.

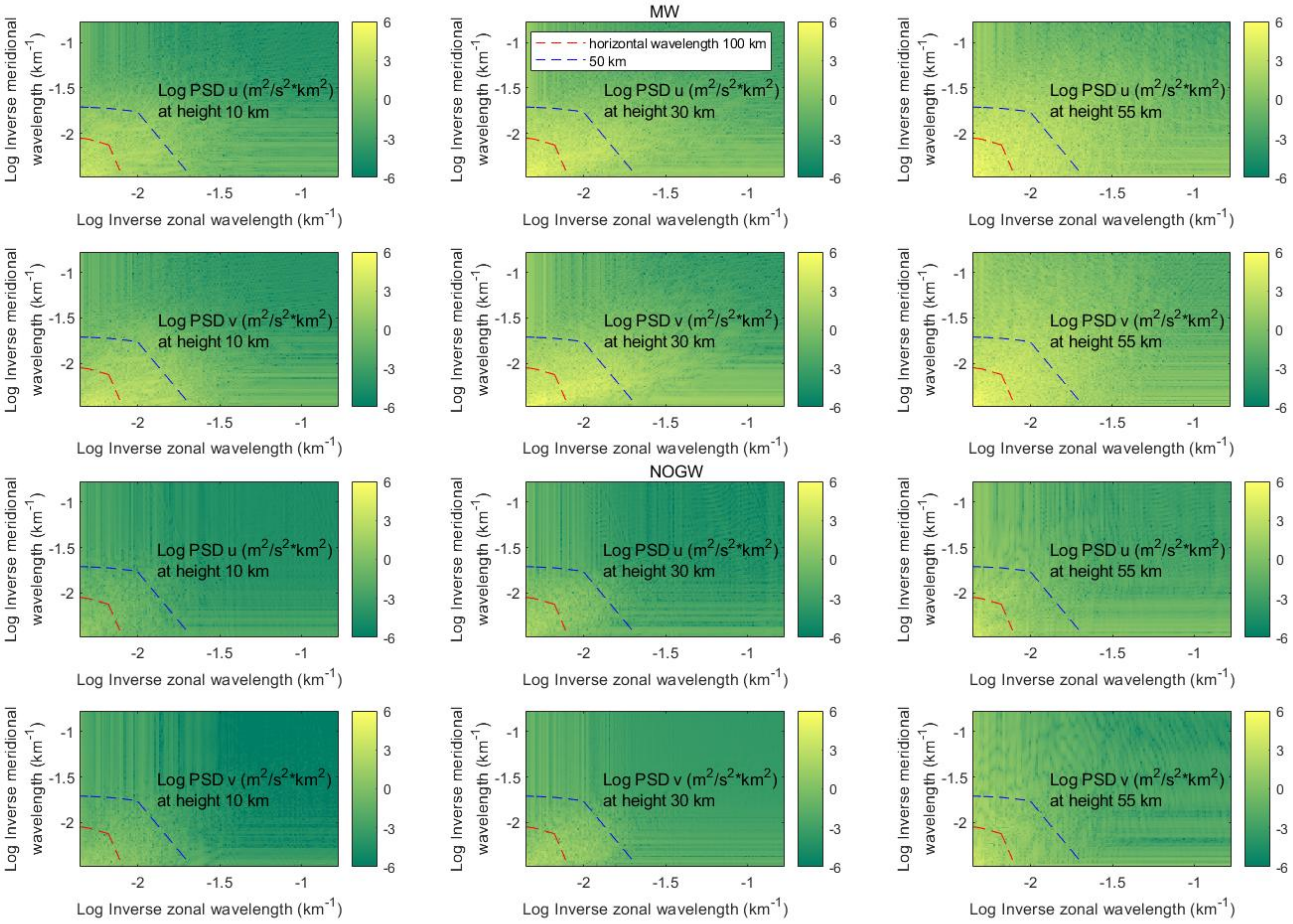

978 **Figure 18.** Two-dimensional power spectral density for both horizontal velocity components at three differ-
979 ent heights on September 12, 00 UTC. The dashed lines show two total horizontal wavelength values (50 and
980 100 km) in terms of the zonal and meridional components. Lower panels refer to NOGW and higher ones to
981 MW.

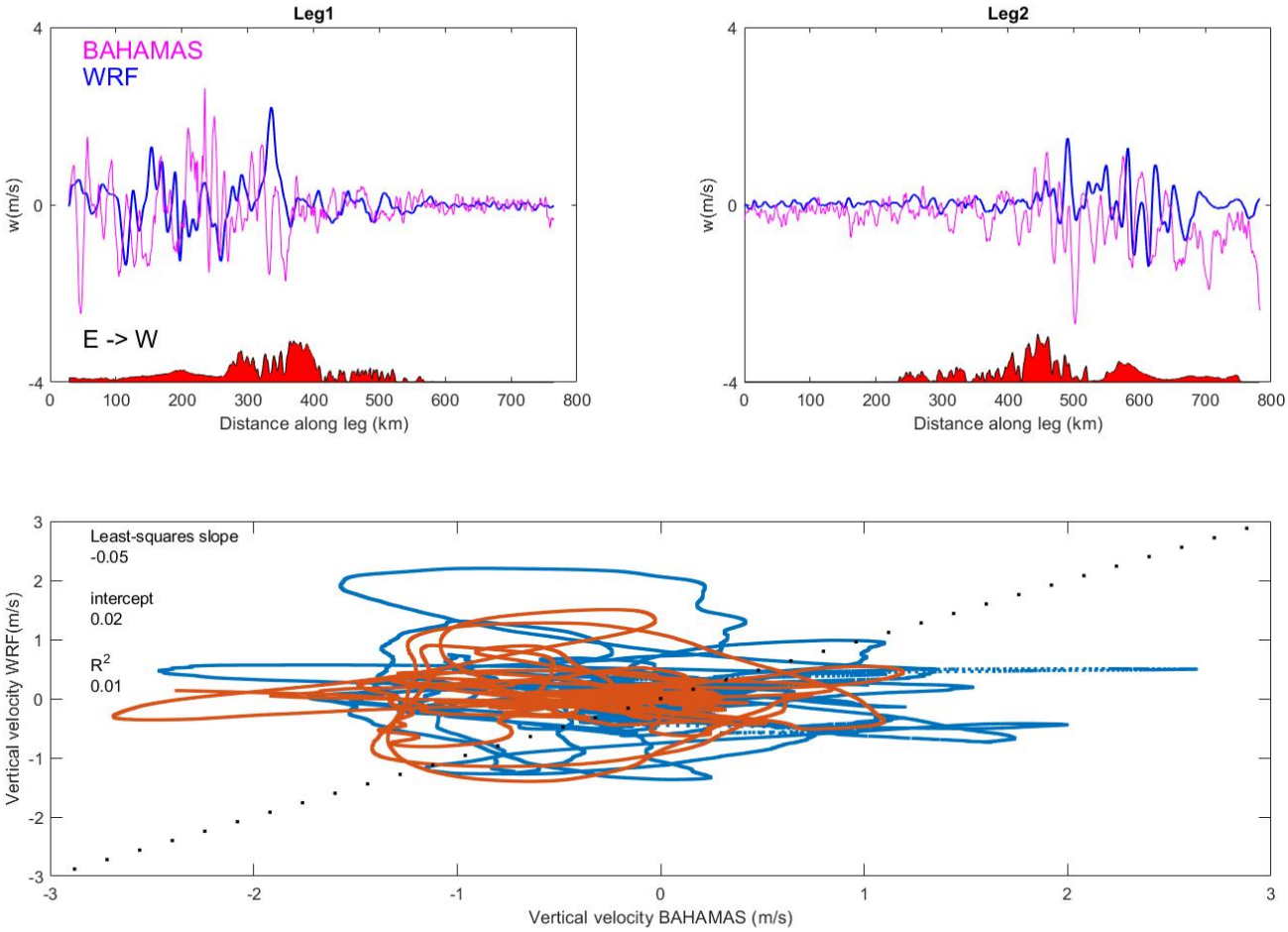

Figure A1. Very high horizontal resolution (1 km) *w* WRF simulations in sectors of legs 1 and 2 around Andes. In the lower panel we show the corresponding comparison against BAHAMAS data at the same time and position with regression results and the identity line.

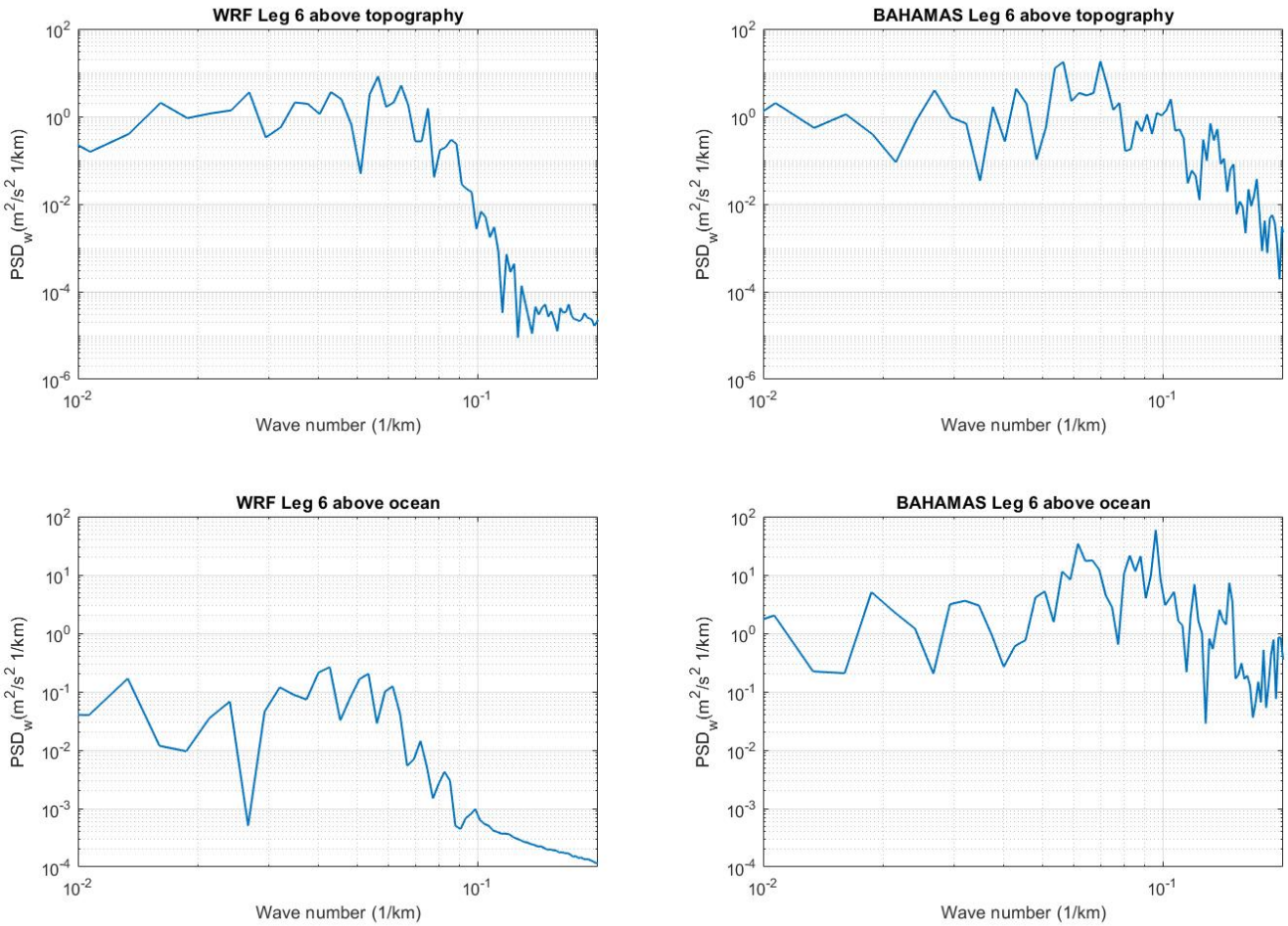

Figure A2. PSD_w for WRF and BAHAMAS data from leg 6 in a first segment above topography and surroundings and the remaining part over the ocean. Wave numbers are obtained from distances along the trajectory.